

1 **Towards Optimal P - T Estimates: An Inverse Method**
2 **for Quantifying P - T Conditions and Uncertainty in**
3 **Phase Equilibrium Modelling**

4 T. Mackay-Champion¹, I.P. Cawood^{1,2}

5 1. Department of Earth Sciences, University of Oxford, South Parks Road, Oxford, OX1
6 3AN, UK.

7 2. NWU-HKU Joint Center of Earth and Planetary Sciences, Department of Earth Sciences,
8 The University of Hong Kong, Pokfulam Road, Hong Kong.

9 Email: ipcawood@gmail.com

10 *Suggested short title: Quantifying uncertainty in Phase Equilibrium Modelling*

ABSTRACT

Phase equilibrium modelling is reliant on quantitative solution models and thermodynamic databases. However, metamorphic studies often employ qualitative to semi-quantitative methods when comparing forward modeled data to the natural datasets that these forward models aim to replicate. These studies frequently overlook, or are unable to quantify, fundamental sources of uncertainty associated with the input data or the technique itself. Accurately constraining these uncertainties is essential for extracting reliable insights from petrological studies and interpreting the data within a well-defined range of confidence. This study introduces an inverse method to quantitatively determine the best-fit P - T conditions and associated uncertainties for a given rock system. The technique computes the difference (misfit) between observed data, such as mineral compositions and/or modal volumes, and forward models across a user-defined P - T grid. The grid point with the lowest misfit value is identified as the best-fit solution. Bootstrap resampling (repeated sampling of the dataset with replacement) enables the user to quantify the uncertainty of the inverse solution. Additionally, three diagnostic metrics—quality of data fit, variable sensitivity, and standard error—are implemented to validate and refine the best-fit solution.

The outlined workflow, LinaForma, is applied on a kyanite-zone pelite (ICSV13) and a garnet+plagioclase-zone metabasite (ICSV117) from the Greater Himalayan Sequence in the Zaskar Himalaya, NW India. The estimated peak P - T conditions and uncertainties for each rock align with results from classical thermobarometric methods, including conventional thermometry, multi-equilibrium barometry, and the pseudosection peak assemblage field. Discrepancies in ICSV117 highlight scenarios where model limitations and/or natural variability may result in different solutions. To assess broader trends in P - T uncertainty in sub-solidus metamorphic conditions, the workflow is then applied to the worldwide median pelite composition of Forshaw & Pattison (2023). The results show that P - T uncertainty varies significantly across metamorphic grade. Lower grades exhibit nearly double the P - T uncertainty of higher grades, with uncertainties ranging from 25–30 °C and 1.2–1.8 kbar at lower-temperature conditions (1 σ , biotite zone and garnet zone) to 16 °C and 0.8 kbar at higher-temperature conditions (1 σ , cordierite/andalusite/staurolite/kyanite zone and sillimanite zone). This pattern is partially mirrored across the facies series, with the highest temperature uncertainty occurring in the lowest-pressure cordierite-andalusite-sillimanite series (1 σ = 29 °C) and the lowest tem-

perature uncertainty in the highest-pressure staurolite-kyanite-sillimanite series ($1\sigma = 16\text{ }^{\circ}\text{C}$), whereas the pressure uncertainty remains relatively constant across all facies series ($1\sigma = 0.9\text{--}1.1\text{ kbar}$).

1 INTRODUCTION

Phase equilibrium modelling is the cornerstone of modern metamorphic petrology, providing a powerful means to decipher the evolution of metamorphic sequences and, in turn, offering critical insights into the processes that shape Earth’s crust and mantle. This modelling relies on large quantitative datasets including thermodynamic end-member properties and activity–composition ($a\text{--}X$) relations of minerals, fluid and melt (e.g., Holland & Powell, 1998). When integrated with appropriate software, these datasets can be used to produce sophisticated forward models that predict equilibrium phase assemblages, compositions, modal volumes, and other such variables across pressure-temperature-composition ($P\text{--}T\text{--}X$) space (e.g., Spear *et al.*, 2016).

Despite the quantitative foundation of these techniques, metamorphic studies predominantly determine the $P\text{--}T$ evolution of a rock using qualitative to semi-quantitative comparisons between the forward modeled predicted outputs and the measured values from the rock (Powell & Holland, 2008). The quality of these comparisons depends on understanding the uncertainties associated with both the modelling process and the input data. As is standard in most scientific fields, any calculation must include a quantifiable estimate of propagated uncertainties, along with a recognition of uncertainties that cannot be quantified (Powell & Holland, 1994, 2008). However, in petrological studies, such uncertainties are often overlooked, such that derived $P\text{--}T$ estimates can not be interpreted within a defined confidence range.

Although several programs employ quantitative approaches for determining optimal $P\text{--}T$ conditions (e.g., Berman, 1991; Gordon, 1992; Powell & Holland, 1994; Duesterhoeft & Lanari, 2020), many of these tools lack direct integration with phase equilibrium modelling, or do not place a strong emphasis on uncertainty quantification. Therefore, our ability to assess the impact of uncertainties on $P\text{--}T$ estimates derived using the latest thermobarometric techniques, remains limited. The aim of this study is to 1) outline the main sources of uncertainty in metamorphic systems, 2) present a new workflow for quantitatively determining the “best-fit” $P\text{--}T$ conditions and associated uncertainty for a given rock system, and 3) quantify the uncertainty across $P\text{--}T$

70 space in a typical pelite (the worldwide median pelite composition; Forshaw & Pattison, 2023)
71 at subsolidus conditions.

2 UNCERTAINTIES

72 In order to account for and quantify uncertainties associated with thermobarometric infor-
73 mation, it is essential to first consider the individual sources of uncertainty. This study recognises
74 four fundamental sources: geological, analytical, parameter, and model, summarised in Figure
75 1. For previous discussions of uncertainties in thermobarometry, see Powell (1985); Hodges &
76 McKenna (1987); Powell & Holland (1988, 1994); Kohn & Spear (1991a, b); Worley & Powell
77 (2000) and Powell & Holland (2008).

78 2.1 Geological uncertainty

79 Geological uncertainty is the non-analytical uncertainty involved in accurately representing
80 the inherent variability of natural systems. These uncertainties may change the accuracy, but
81 not precision, of the result. Specifically, this stems from sampling bias, the interpreted scale
82 of equilibrium, disequilibrium processes, and selection of the equilibrium assemblage (Figure
83 1).

84 Sampling bias and natural inhomogeneity contribute to uncertainties in the measured (or
85 calculated) bulk composition due to petrological differences between samples, such as variations
86 in mineral abundances or compositions. Additionally, the method used to determine bulk com-
87 position can vary depending on the interpretation of the scale and degree to which equilibrium
88 has been achieved within the mineral assemblage. For instance, XRF analysis assumes that
89 chemical equilibrium is achieved at the scale of the entire ‘rock’, producing a ‘total’ bulk compo-
90 sition. However, many metamorphic rocks preserve chemical zoning in porphyroblasts, meaning
91 that an ‘effective’ bulk composition derived from a smaller-scale analysis, such as from point
92 counting and compositional analysis of a thin section, may be more appropriate. Uncertainty in
93 the bulk composition can have a profound effect on the topology of a pseudosection (e.g., Stüwe
94 & Powell, 1995; Stüwe, 1997; Guevara & Caddick, 2016; Palin *et al.*, 2016; Lanari & Engi, 2017).
95 On a sample-specific basis, this uncertainty can be estimated using replicate blocks (Palin *et al.*,
96 2016) or variable domains within the selected volume (Duesterhoeft & Lanari, 2020).

97 The equilibrium-based framework of thermodynamics is inherent to forward modelling the

98 consequences of metamorphic transformation at fixed P - T - X conditions. However, kinetic
99 factors—such as reaction affinity and diffusion rates—may influence whether a sample achieves
100 equilibrium over the length scale of interest (e.g., Thompson, 1986; Waters & Lovegrove, 2002;
101 Pattison & Tinkham, 2009; Pattison & Spear, 2018; Starr & Pattison, 2019). Consequently,
102 many rocks preserve multiple equilibria, herein disequilibrium, which often provides more de-
103 tailed information about the P - T evolution of a sample than a rock that has achieved perfect
104 chemical and textural equilibrium (e.g., Carlson *et al.*, 2015). Although an assessment of equi-
105 librium can be made through careful observational criteria in thin sections and compositional
106 phase analyses, it is impossible to definitively prove. By necessity, studies must account for
107 varying scales of disequilibrium and carefully define the spatial or volumetric extent over which
108 equilibrium assumptions are valid.

109 The phases chosen to inform the interpreted equilibrium assemblage and bulk composition
110 are critical: including ambiguous minerals may distort the interpretation, whilst omitting key
111 phases can yield an incomplete representation. Additional uncertainties arise when attempting
112 to match the interpreted equilibrium assemblage and mineral measurements with those of the
113 predicted model result. The predicted result may be reliant on assumptions in the formulation of
114 the model which are not always consistent with natural data (e.g., Forshaw *et al.*, 2019; Waters,
115 2019). Therefore, the phases chosen to prioritise when comparing the natural observations and
116 model predictions will inevitably bias the solution. For example, the presence or absence of
117 small modal volume or accessory phases (e.g., Fe-Ti-oxides) should be treated with particular
118 caution in defining the peak assemblage of the forward model, as they contribute very little to
119 the overall Gibbs free energy of the assemblage and require implausible precision from the a - X
120 models (Weller *et al.*, 2024).

121 Although geological uncertainties are largely non-systematic, statistical approaches have
122 been proposed to evaluate the impact of quantifiable geological uncertainties (Figure 1) on
123 estimated P - T conditions or corresponding mineral properties (Steltenpohl & Bartley, 1987;
124 Hodges & McKenna, 1987; Palin *et al.*, 2016; Forshaw *et al.*, 2019). For example, even moderate
125 uncertainties in modal mineral proportions due to natural petrographic variation can result in
126 displacements of phase boundaries by approximately ± 1 kbar (Palin *et al.*, 2016).

127 2.2 Analytical uncertainty

128 Analytical uncertainty is the uncertainty in the measurements derived from data acquisition,
129 processing, and calibration. This may affect the accuracy and precision of the result. Analytical
130 uncertainty affects measured mineral compositions, modal abundances, whole-rock composition,
131 and other non-standard rock or mineral properties such as XFe^{3+} (Figure 1). The first two are
132 explored here. This data is influenced by the geological uncertainty.

133 Analysis of mineral compositions via techniques such as electron probe microanalysis
134 (EPMA) involves uncertainties on the measured weight percent oxide values derived from count-
135 ing statistics, standardisation, and correction procedures. Uncertainties of these kind are treated
136 routinely and may be negligible if undertaken at a single analytical facility (Worley & Powell,
137 2000). The measured weight % oxides are subsequently recalculated as cations per formula unit,
138 then the mole fractions of end-members are determined by normalising groups of recalculated
139 cations to the expected number of cations on the specific crystallographic site. However, the
140 direct propagation of relative uncertainties on weight % oxides into resulting uncertainties on
141 mole fractions produces substantial correlation among the mineral components (Kohn & Spear,
142 1991b). Therefore Monte Carlo procedures are preferred to estimate uncertainties on the cal-
143 culated mole fractions (e.g., Hodges & McKenna, 1987; Steltenpohl & Bartley, 1987; Kohn &
144 Spear, 1991b).

145 Determining the modal abundance of minerals also includes uncertainties. Routinely used
146 approaches to determine modal abundance include point counting and automated mineralogical
147 analysis (via EPMA or scanning electron microscope). Factors that contribute to uncertainty
148 include features such as the point size/image resolution, amount of each mineral, the grain
149 size and shape, the spacing between points, and the number of points calculated. Automated
150 mineralogical analysis are also subject to their own analytical uncertainties which may include
151 classification algorithms, and thresholds used to distinguish mineral phases. Approaches to
152 estimate these uncertainties include statistical methods assuming a binomial distribution based
153 on the amount of each mineral and the number of points calculated (Van der Plas & Tobi, 1965)
154 and bootstrap resampling (Evans & Napier-Munn, 2013; Blannin *et al.*, 2021).

2.3 Parameter uncertainty

Parameter uncertainty is the uncertainty in the forward model predictions as a result of user-selected input parameters. These choices may affect the accuracy of the result. This includes the choice of thermodynamic databases, a - X models, model system, and input parameters like $X_{\text{Fe}^{3+}}$, fluid composition, and water content (Figure 1). These choices are often influenced by both analytical and geological uncertainty.

Although ds6.2 (Holland & Powell, 2011) represents a significantly expanded and refined dataset, disagreements remain regarding which thermodynamic database and a - X models best reproduce natural observations (e.g., Pattison & DeBuhr, 2015; Waters, 2019; Gervais & Trapy, 2021; Pattison & Goldsmith, 2022). The choice of a model system is also critical. A system too small to fully capture the controlling equilibria may fail to reproduce observed mineral assemblages, mineral compositions, or modal abundances (White *et al.*, 2007). Simplified model systems often omit minor elements present in natural rocks (e.g., Zn in staurolite), which can significantly affect the stability of certain minerals. Conversely, including minor elements can introduce other problems, such as inadequate partitioning of added components across multiple solution models, which may artificially over-stabilize select phases, thereby impacting the composition and abundance of other assemblage phases. It is often not possible to compare the impact of these omissions or additions. However, the addition of Mn to the model system is shown to strongly impact the stability of garnet with changing P - T conditions, with minimal changes to other common pelitic minerals or the overall topology (Tinkham *et al.*, 2001; White *et al.*, 2007). The precision and boundary range of the model system can also impact whether the desired phase information is calculated.

Several other key input parameters introduce additional uncertainties, including the ferric-to-ferrous iron ratio ($X_{\text{Fe}^{3+}}$), total H_2O in the system ($M\text{H}_2\text{O}$), and fluid composition ($a\text{H}_2\text{O}$). The oxidation state of a rock, expressed as the ratio of ferrous (FeO , Fe^{2+}) to ferric (Fe_2O_3 , Fe^{3+}) iron, strongly affects phase equilibria and has been a key parameter in thermobarometric studies (Schumacher, 1991; Diener & Powell, 2010; Forshaw *et al.*, 2019). Despite its significance, routine bulk composition analyses (e.g., XRF, EPMA) cannot distinguish between Fe^{3+} and Fe^{2+} . Methods such as charge balancing, the “flank method”, and empirical estimates can infer Fe^{3+} and Fe^{2+} for some minerals (e.g., garnet, pyroxene, amphibole; Droop, 1987; Hofer *et al.*, 1994; Holland & Blundy, 1994; Hawthorne *et al.*, 2012), but are ineffective for minerals with

186 structural vacancies (e.g., biotite, white mica, chlorite, staurolite; Schumacher, 1991). Without
187 costly techniques like wet chemical titration, Mössbauer spectroscopy, or XANES, $X\text{Fe}^{3+}$ is often
188 estimated using literature values or by exploring P - X and T - X pseudosections (e.g., Doukkari
189 *et al.*, 2018; Schorn & Diener, 2019).

190 For sub-solidus conditions, fluid-present systems are typically assumed to contain excess
191 H_2O during prograde metamorphism (Guiraud *et al.*, 2001). In supra-solidus conditions, water
192 content must often be estimated, with approaches varying based on the portion of metamorphic
193 history being modeled. These different approaches substantially impact pseudosection topology
194 and predicted melt content (see discussion in Waters, 2019). Under fluid-present sub-solidus
195 conditions, devolatilisation reactions using pure H_2O are assumed to dominate. However, where
196 fluid composition-dependent conditions are implicated, a lower $a\text{H}_2\text{O}$ may be necessary (e.g.,
197 Ohmoto & Kerrick, 1977), which shifts the temperature of mineral assemblage boundaries and
198 the solidus (e.g., Weller *et al.*, 2013).

199 2.4 Model uncertainty

200 Model uncertainty is the uncertainty inherent in forward model predictions stemming from
201 the data, algorithms, and choices used to formulate the model. This may impact both the
202 accuracy and precision of the predicted results. This should be understood separately from
203 parameter uncertainty, which is related to user-choices. Uncertainties derived from the under-
204 lying thermodynamic dataset and a - X relations play a particularly important role in model
205 uncertainty (Figure 1).

206 For single-reaction thermometers and barometers, these uncertainties are dominantly ex-
207 pressed by the precision of the experimentally or empirically determined end-member reac-
208 tions and thermodynamic parameters used in calibration (Hodges & Crowley, 1985; Hodges &
209 McKenna, 1987; Kohn & Spear, 1991a). However, for multi-equilibrium thermobarometry and
210 phase equilibrium modelling, the uncertainties are associated with the thermodynamic proper-
211 ties of the individual mineral end-members (Worley & Powell, 2000) and the calibrations used
212 will adjust within error brackets to ensure values are internally consistent (Holland & Powell,
213 1998, 2011). For these thermodynamic datasets, the uncertainties on, and correlations between,
214 the enthalpies of formation are determined by least-squares derivation from the experimental
215 data (Powell & Holland, 1993a). Such uncertainties and correlations can be propagated through

the dataset onto calculated values of P and T (avPT; Powell & Holland, 1988, 1994). The other thermodynamic properties (e.g., entropy and molar volume) are treated as relatively well-constrained in the derivation, as they can be measured or estimated with greater confidence. However, uncertainties in activity-composition relationships and analytical measurements may introduce additional uncertainties of comparable or greater magnitude than those stemming from enthalpy uncertainties (Powell & Holland, 1988).

The complexity of minerals, in terms of crystal structure and the differences of site preferences for atoms during mixing, means solution (a - X) models are necessarily simplifications from natural systems (Powell & Holland, 1993b). The formulation of a - X relations (see Powell & Holland, 1993b; Holland & Powell, 1996a, b, 2003) treats mineral phases as solid solutions composed of independent end-members, allowing for a range of possible ordering states (Holland & Powell, 1996a). Despite the nonideality characteristic of many minerals, the complexity of accounting for such features may be impracticable and therefore, where required, ideality is assumed (Powell & Holland, 1993b). Normalisation is applied to ensure that both the ideal mixing activity and the activity coefficient for each pure end-member are set to unity, allowing solution models to be created even for minerals such as hornblende containing complex multi-site phases (Powell & Holland, 1993b). However, the difficulty in constraining the activity coefficients and interaction parameter terms carries large uncertainties into a - X relationships, and the lack of a - X data for minerals makes it challenging to constrain these associated uncertainties (Powell & Holland, 1988). An attempt to include realistic uncertainties is detailed in Powell & Holland (1988), where the uncertainty on the endmember activity is dominated by the cation site with the largest normalised uncertainty, even in a complex formula unit. The decisions taken formulating these models for certain minerals (e.g., distortion of Al/Si charge balance, or not incorporating vacancies in octahedral and interlayer sites) inevitably impact how they reproduce natural compositions for the whole assemblage, and the scale of this impact will vary across P - T space (Forshaw *et al.*, 2019; Waters, 2019; Dubacq & Forshaw, 2024).

2.5 Combined uncertainties and correlations

A total uncertainty, derived from the summation and propagation of the outlined uncertainty sources, remains hypothetical due to the incomplete nature of propagation (Powell & Holland, 1988; Kohn & Spear, 1991b), and the inability to fully quantify all uncertainties (Figure 1). As a result, any solution uncertainties represent only the partial propagation of select quantifiable

sources, offering a minimum estimate (Powell & Holland, 2008). Furthermore, the inherent interdependence of these uncertainties means that quantitative uncertainty estimates are not entirely independent; instead, they encapsulate contributions from multiple, mutually dependent sources. This interdependence within the modeled system means changes to the system are multifaceted in effect. For example, displacements of key field boundaries are correlated such that the a - X relations used in thermodynamic modeling should consistently reproduce the correct sequence of up-temperature or up-pressure assemblages (Green *et al.*, 2016).

Despite the complex relationship between uncertainties, quantitative assessments remain essential for understanding the relative scale and impact of these uncertainties. A comprehensive assessment of the scale of all the quantifiable uncertainties (Figure 1) is beyond the scope of this study. However, it is understood that imprecisely known activity-composition relationships and geological or analytical uncertainties contribute a greater uncertainty than those stemming from dataset enthalpies, which is the primary source of uncertainty considered within the thermodynamic models (Powell, 1985; Powell & Holland, 2008). For “predictive” uncertainties (e.g., thermodynamic dataset and end-member activities, Figure 1), the user can employ the *avPT* methods outlined by (Powell & Holland, 1988, 1994). This study focuses on quantifying “observational” uncertainties (those stemming from uncertainty in the mineral measurements and/or bulk rock composition, Figure 1), though the outlined method will inherently account for some degree of these systematic uncertainties derived from the predictions.

3 INVERSION METHOD

Forward modelling is the process of predicting the data one would observe for a given set of model input parameters. A pseudosection is an example of a forward model, in which the equilibrium phase assemblage, phase compositions, and abundances are predicted for a rock of a given composition across P - T space. This is contrasted with inverse modelling in which observed data is used to estimate the underlying model parameters. Conventional thermobarometry (e.g., Ti-in-biotite geothermometer; Henry *et al.*, 2005) and multi-equilibrium thermobarometry (Powell & Holland, 1994) are examples of inverse methods, where P - T conditions are estimated from the observed mineral measurements.

Constraining the conditions of equilibration and evolution of a rock from a forward model is typically achieved using intersecting isopleths of phase compositions or modal volumes, cal-

culated using phase equilibrium modelling. This method has been effectively applied to semi-quantitatively analyze the tectonothermal evolution of geological terranes (e.g., Vance & Mahar, 1998; Hoschek, 2004; Štípská & Powell, 2005). In its simplest form, this can involve using a mean or representative analysis from two variables to determine a singular point of cross over in P - T space (Figure 2a). Alternatively, the observed data distribution of two or more variables may define varying zones of overlap (Figure 2b, c, d). In all cases the accuracy and precision of the resulting P - T estimates, and thereby the conclusions drawn from the sample, are significantly influenced by the variables selected (Figure 2a, b, c, d). The selected variables will have differing population distributions and differing sensitivity to P - T changes. Even a narrow observed population distribution can correspond to a broad calculated P - T interval if the variable is highly responsive to P - T changes (Figure 2b). Including, additional variables may make for a more “representative” result, but can also result in multiple zones of overlap (Figure 2c), or poor to no agreement (Figure 2d). Such approaches are often ultimately influenced by selection bias, choosing the variables that show best agreement for the expected conditions of equilibration.

The workflow presented in this study, LinaForma, aims to address these challenges by applying a new inverse method that allows for the simultaneous inversion of a large set of variables (Figure 2e). By using a grid-search inversion coupled with bootstrap resampling of the mineral measurements, the workflow calculates the “best-fit” P - T conditions and associated uncertainties for a given bulk rock composition. A schematic of the workflow is shown in Figure 3. This workflow is then applied to a kyanite-zone pelite (ICSV13) and a garnet+plagioclase-zone metabasite (ICSV117) from the Greater Himalayan Sequence in the Zaskar Himalaya, NW India (Figure 5). As a large number of mineral composition variables are used in this study, their definitions are included in Table 1 for reference.

3.1 Best-fit P - T conditions: the grid-search inversion

This workflow uses a grid-search inversion to determine the optimal or “best-fit” P - T conditions for a given rock system. The grid-search involves drawing a large number of trial solutions from a regular grid in model (P - T) space. For each point on the grid (i.e., a trial solution), the difference between the forward model’s predicted data and the observed data is computed using an objective, or misfit, function (Figure 3a). The best-fit solution is the point on the grid with the lowest value of the misfit function. In this case, the observed data may include

307 mineral composition, mineral modes, and bulk properties such as the interpreted equilibrium
308 phase assemblage and whole-rock density. The forward models for each point on the grid can
309 be calculated using programs such as THERIAK-DOMINO (de Capitani & Brown, 1987; de
310 Capitani & Petrakakis, 2010), Perple_X (Connolly, 1990, 2005), and MAGEMin (Riel *et al.*,
311 2022), which rely on Gibb’s free energy minimisation to determine the most stable equilibrium
312 assemblage as a function of P , T , and X .

313 This workflow uses the L1-norm misfit function (f), equivalent to the sum of absolute
314 residuals (Equation 1).

$$f = \sum_{i=1}^N \frac{|x_i^{\text{obs}} - x_i^{\text{mod}}|}{x_i^{\text{obs}}} \quad (1)$$

315 Where N is the total number of variables, x_i^{mod} is the value of variable i predicted at the
316 trial solution, and x_i^{obs} is the observed value of variable i . The residuals are scaled relative to
317 the observed value of each variable to ensure that variables with large magnitudes do not have
318 an overwhelming influence on the result. Large values of f suggest the model predictions poorly
319 fit the observed data, whilst low values of f show the observed data and the model predictions
320 are similar (i.e., the data “residuals” are small). The trial solution with the lowest value of f is
321 the best-fit solution.

322 3.2 Uncertainty analysis: bootstrap resampling

323 Bootstrap resampling is used to estimate of the uncertainty associated with the best-fit
324 P - T solution. This involves resampling the observational data with replacement, and then
325 computing the required statistics for each resampled dataset, in this case the best-fit solution
326 of the grid-search inversion (Figure 3b). When repeated multiple times (e.g., $N \geq 1000$), the
327 distribution of inversion solutions obtained from the resampled datasets provides an estimate
328 of the true mean or median solution and the population distribution (Menke, 1984). Bootstrap
329 resampling can be either non-parametric or parametric. Non-parametric bootstrapping involves
330 resampling with replacement from the original observational dataset. Parametric bootstrapping
331 generates samples according to an assumed distribution of the observational data (Efron, 1979),
332 in this case a normal distribution (Figure 3b). Given the non-Gaussian nature of the probability
333 density function in non-linear problems (Menke, 1984), percentile-based confidence intervals such

as the interquartile range are often more informative than the standard deviation. Bootstrap-resampling is also used to assess the sensitivity of the inversion results to uncertainty in each variable (Section 3.3.2, Figure 3c).

3.3 Diagnostics

The workflow includes three diagnostics with which to validate and refine the best-fit solution: (1) Quality of data fit (X_{total}) between the best-fit solution and the observations; (2) the sensitivity of the best-fit solution to each of the chosen variables; and (3) the standard error (SE). The values of these diagnostic metrics are automatically output in table format at the end of the inversion calculations. The definitions for each value in the diagnostics table are included in Table 2.

3.3.1 Quality of data fit (X_i , X_{total})

The data fit metric assesses the level of agreement between the median best-fit solution and the observations. This is quantified by assessing whether the model’s predictions at the median best-fit conditions (e.g., the modeled value of X_{Alm} garnet at PT_{best}) fall within two standard deviations of the observed values. This assessment is provided in the workflow by a score for each variable (X_i) and a total score (X_{total}). These are calculated following Equations 2 and 3 respectively.

$$X_i = \frac{|x_i^{\text{obs}} - x_i^{\text{mod}}|}{2\sigma_i^{\text{obs}}} \quad (2)$$

$$X_{\text{total}} = \frac{1}{N} \sum_{i=1}^N X_i \quad (3)$$

N is equal to the total number of variables, X_i^{mod} represents the value of variable i predicted at the best-fit solution, X_i^{obs} represents the observed value of variable i , and σ_i^{obs} represents the observed standard deviation for variable i . A value of > 1 for both the total score and the individual variable scores indicates a poor fit. A total score of ≤ 1 demonstrates that the inversion fits the data acceptably well, and an individual variable score of ≤ 1 indicates that the modeled prediction fits the observations within 2 standard deviations. The workflow provides options to visualize this relationship (e.g., Figure 4d). The scoring strategy above provides a metric similar to the σ_{fit} metric (square-root of the Mean Square Weighted Deviation) in Powell

360 & Holland (1994).

361 3.3.2 Sensitivity (ΔP , ΔT)

362 Sensitivity analysis evaluates how uncertainty in input variables affect the inversion result.
363 This is performed using bootstrap resampling, in which each variable is resampled in turn while
364 the remaining variables are fixed at the appropriate mean value (Figure 3c). The resultant spread
365 in the best-fit solutions can then be linked directly to variation in the resampled variable. The
366 sensitivity values are given as the maximum absolute temperature (ΔT_i) and pressure (ΔP_i)
367 difference between the mean solution of the inversion when all the variables are re-sampled
368 ($T^{\text{median}}, P^{\text{median}}$) and the range of solutions when only a single variable (i) is re-sampled n
369 times ($T_i^{\text{min}} - T_i^{\text{max}}, P_i^{\text{min}} - P_i^{\text{max}}$).

$$T_i^{\text{max}} = \text{mean}(T_i^n) + 2 \times \text{std}(T_i^n) \quad (4)$$

$$T_i^{\text{min}} = \text{mean}(T_i^n) - 2 \times \text{std}(T_i^n) \quad (5)$$

$$\Delta T_i = \max |(T^{\text{mean}} - T_i^{\text{min}}), (T_i^{\text{max}} - T^{\text{mean}})| \quad (6)$$

372 Where T_i^n is the distribution of best-fit temperatures from the re-sampling of variable i . The
373 same equations apply for pressure. The comparison is made with the mean solution rather than
374 the median solution because the mean is less sensitive to the discretization of the model grid.
375 A high sensitivity may be caused by a large spread in the value of observed data variables, or a
376 large percentage change in the model values over small areas of P - T space (meaning that small
377 differences in input value results in a large change in pressure or temperature estimate). This
378 analysis is often displayed using tornado plots (e.g., Figure 4e). The sensitivity analysis provides
379 a similar function to the dimensionless hat value (also called the leverage value) used to quantify
380 the influence of individual end-members on the final result in avPT (Belsley *et al.*, 1980; Powell
381 & Holland, 1994). However, the values calculated by this workflow are in units of temperature
382 and pressure.

383 3.3.3 Standard error (SE)

384 The standard error (SE) metric quantifies the extent to which the mean result of the inver-
385 sion is expected to deviate from the true population mean (i.e., how close the estimated best-fit

386 solution is to the “true” solution; Equation 7).

$$SE = \frac{\sigma}{\sqrt{N}} \quad (7)$$

387 Where N is the number of variables, and σ is the standard deviation of the bootstrap solutions
388 for both pressure and temperature, respectively. A smaller SE value indicates that the sample
389 mean is a more precise estimate of the population mean. Increasing the number of data variables
390 (i.e., N) used within the inversion will typically reduce the SE.

391 3.4 Applying the workflow

392 3.4.1 Observations setup

393 Any variable can be used in the inversion provided an appropriate forward model can be
394 calculated, and the data can be tabulated into grid format. The type of variables (e.g., mineral
395 compositions and/or modal volumes) employed during the inversion should reflect the interpreted
396 scale of chemical and textural equilibrium and the method of bulk composition acquisition.
397 Table 1 lists recommended compositional variables for pelitic and metabasic lithologies in sub-
398 solidus systems. For any major phase with a relevant solution model, and variables that can
399 provide robust P - T constraints, at least one variable should be included to ensure the misfit
400 function accommodates its presence. A degree of freedom should always be preserved (e.g., for
401 plagioclase, X_{An} and X_{Ab} should not both be included—one is sufficient to fully describe the
402 system). Modal volume variables may be used for major volume phases but should be treated
403 with caution or avoided for minor volume or accessory phases (Weller *et al.*, 2024). A minimum
404 of three variables, ideally from more than one phase, should be used for any inversion. An
405 exception to this guideline may apply to garnet, where core compositions can be interrogated
406 independently. The inferred peak assemblage field is not inherently enforced as a constraint
407 unless used directly as a variable or stable phases are explicitly assigned a non-zero volume (or
408 vice-versa). The advantages and limitations of this decision are further discussed in Section
409 6.2.2.

410 If the bulk rock composition varies significantly across the analysed rock volume, this un-
411 certainty can be assessed by computing a range of forward models calculated for Monte-Carlo
412 variations in the input composition (Section 5.2). This range can be defined using various
413 approaches, including replicate blocks or an uncertainty level characteristic of a type assem-

414 blage(Palin *et al.*, 2016), resampling from discrete bulk composition domains within a thin
415 section (e.g., Duesterhoeft & Lanari, 2020), or an uncertainty level characteristic of the scale of
416 variation (e.g., 5%; Forshaw *et al.*, 2019).

417 3.4.2 Predictions setup

418 The P - T grid must be sufficiently broad to avoid boundary effects influencing the best-fit
419 solutions whilst maintaining precision to capture the true solution between grid points. If results
420 converge on the boundary of the P - T range, a different range should be chosen. The spacing
421 should align with the precision of both input data and the forward model. As a general guideline,
422 the grid spacing should not exceed 10 °C and 100 bar.

423 The method of bootstrap resampling should be chosen based on the data distribution or
424 availability. Parametric bootstrapping, using a mean and standard deviation, is suitable for
425 normally distributed data, while non-parametric bootstrapping, using the original data, is more
426 appropriate for non-normal data. A minimum of 1000 bootstrap resamples is recommended,
427 though the exact number should be verified by observing the distribution of the P and T
428 solutions against the number of bootstrap re-samples (Figure S1). The distribution of solutions
429 should have stabilized prior to the selected number of bootstraps.

430 3.4.3 Result interrogation

431 Prior to inversion, the relationships of different variables in P - T space should be interrogated
432 to assess whether mutual equilibrium is likely for the selected variables and whether appropriate
433 modelling parameters (P - T range, XFe^{3+} , etc.) have been used. This can be visualized for all
434 variables (e.g., Figure 4a) or for individual variables (e.g., Figure 4b). A preliminary assessment
435 of mutual equilibrium can be made, and variables may be filtered to exclude any that may stem
436 from clear geological or model uncertainty. However, in most cases it is preferable to let the
437 variables be removed through the diagnostics.

438 Fit diagnostics provide critical insight into the reliability of inversion results (Table 2).
439 If the total score of the quality of data fit (X_{total}) is above 1, variables with fit scores (X_i)
440 exceeding 1 should be removed sequentially, starting with the most severe, until X_{total} falls
441 below or is equal to 1. Further variables need not be removed to reduce the score. High
442 sensitivity values (ΔP , ΔT) are not inherently problematic unless coupled with poor fit scores.

443 For example, X_{total} may be at or below 1 whilst several individual variables show X_i scores
 444 well above 1. In these instances, if the sensitivity values of the individual variables are greater
 445 than approximately 2 % of the best-fit result (Table 5), consider removing the poorly fitting
 446 variables. This occurs infrequently, as the L1-norm function is robust to outliers (Claerbout &
 447 Muir, 1973; Li *et al.*, 2015; Ibraheem *et al.*, 2021). Persistent scatter among variables, rather
 448 than isolated outliers, may indicate disequilibrium or retrogression (Powell & Holland, 1994),
 449 and in such cases sequential removal might not resolve the issue. Finally, the standard error
 450 (SE) of the solution should be minimized as much as possible by incorporating the maximum
 451 possible number of robust variables in the inversion.

452 The best-fit solution and associated uncertainty should ideally overlap the interpreted peak
 453 assemblage field. Discrepancies may indicate inconsistencies in the analyzed rock volume across
 454 different techniques, the scale of equilibrium, or the definition of the equilibrium assemblage. In
 455 some instances, the bootstrap re-sampling may highlight the possibility of multi-modal results.
 456 The distribution of the solution uncertainty can be assessed using histograms or the heatmap
 457 of solutions (Figure 4c). In this case, the user could either add additional observations to help
 458 further constrain the solution or assess the merits of the various solutions based on independent
 459 constraints such as conventional thermobarometers. Significant local minima will also result in
 460 an increase in estimated uncertainty, as indicated by a higher interquartile range.

461 **3.4.4 Result reporting**

462 Results should generally be reported using the median and inter quartile range (IQR), as
 463 these metrics are suitable for non-normal distributions. The heatmap of solutions (e.g., Figure
 464 4c) should be accompanied by a pseudosection. A diagnostic table (e.g., Tables 2, 5) summarizing
 465 the best-fit solutions, uncertainty (IQR, standard error), and quality of fit for each individual
 466 variable as well as the inversion as a whole must also be provided. Given that the results depend
 467 on key parameters such as bootstrap type, number of bootstraps, grid range, and grid precision,
 468 this information should be clearly documented. Additionally, visual aids like overlap percentage
 469 plots or sensitivity tornado plots may be valuable for various applications.

4 NATURAL EXAMPLES

4.1 Sample descriptions

To demonstrate the applicability of the workflow, mineral compositions (collected via EPMA) of a kyanite-zone pelite (ICSV13) and a garnet+plagioclase-zone metabasite (ICSV117) from the Greater Himalayan Sequence in the Zaskar Himalaya, NW India, were inverted to determine best-fit P - T conditions and compared with classical thermobarometric methods. The analytical setup, mineral recalculation procedure, formulation of bulk composition, and forward modelling procedure are included in the Supplementary Text. The bulk rock composition was collected using XRF, assuming chemical equilibrium was achieved at the 'rock-scale', the measured composition for both samples is included in Table 3. The input and forward model for each sample are included in the Supplementary material (Tables S1–S4).

ICSV13 contains the assemblage muscovite, biotite, quartz, kyanite, garnet, staurolite, and plagioclase. Accessory phases include apatite, chlorite, rutile, ilmenite, graphite, tourmaline, and monazite. A characteristic photomicrograph of the relevant minerals and textures is located in Figure S2a. Kyanite occurs as prismatic subhedral poikiloblasts throughout the section, whereas, staurolite appears as a singular large prismatic poikiloblast ($X_{\text{Mg}} = 0.19$ – 0.20). Both minerals overgrow the matrix fabric, display impinged grain boundaries variably defined by each other, and share a concordant inclusion trail with the same inclusion assemblage (Figure S2a). Garnet occurs as rounded to flattened subhedral poikiloblasts with strong compositional zoning ($X_{\text{Alm}} = 0.60$ – 0.76 , $X_{\text{Prp}} = 0.05$ – 0.16 , $X_{\text{Sps}} = 0.19$ – 0.02 , $X_{\text{Grs}} = 0.16$ – 0.06). Biotite and muscovite define the dominant matrix fabric. Analysed biotite grains are compositionally homogenous ($X_{\text{Mg}} = 0.49$, Ti apfu = 0.09 – 0.11), whereas muscovite shows some compositional variation (Si apfu = 3.04 – 3.09 , $X_{\text{Cel}} = 0.07$ – 0.09 , $X_{\text{Pa}} = 0.21$ – 0.25). Locally weakly oriented to unoriented chlorite overgrows biotite. Plagioclase occurs as oval subhedral to anhedral grains and shows some variation across the albite–oligoclase compositional boundary ($X_{\text{Ab}} = 0.84$ – 0.92). Ilmenite, forms coarser grains along kyanite and garnet boundaries. Both rutile and ilmenite occur as inclusions in peak porphyroblasts. The inferred equilibrium assemblage at peak conditions for ICSV13 is kyanite-staurolite-garnet-biotite-muscovite-plagioclase-quartz-rutile-ilmenite- H_2O .

ICSV117 contains the assemblage hornblende, plagioclase, biotite, and quartz. Accessory phases include titanite, chlorite, apatite, and ilmenite. A characteristic photomicrograph of

the relevant minerals and textures is located in Figure S2b. Amphibole occurs as coarse acicular prismatic grains and classified as magnesiohornblende–pargasite (Hawthorne *et al.*, 2012). Vectors vary as follows: tschermakite from 0.97–1.19, edenite from 0.25–0.55, and glaucophane from 0.12–0.21. Biotite is present as coarse subhedral poikiloblasts to fine tabular grains with a homogenous composition (X_{Mg} of 0.48–0.52, Ti of 0.14–0.16 apfu). Minor chlorite occurs in replacement of biotite. Plagioclase occurs as oval to angular prismatic euhedral–subhedral grains. Strong concentric compositional zoning is locally observed. Plagioclase is defined as oligoclase (X_{Na} of 0.77–0.81). Ilmenite and titanite are the main Ti-oxide phases. Ilmenite form individual crystals, whereas titanite form polycrystalline string-of-beads textures, ilmenite occur as cores to titanite rims, though both are in contact with the matrix. Ilmenite grain boundaries is defined by shape habit of amphibole, whereas titanite, commonly forming along amphibole crystals, locally impinge amphibole grain boundaries. The inferred equilibrium assemblage at peak conditions for ICSV117 is: hornblende-biotite-plagioclase-quartz-ilmenite-titanite- H_2O .

4.2 ICSV13

4.2.1 Conventional methods of analysis

Given the inferred peak assemblage, an approximation of the peak field could be represented by either 1) the staurolite-stable field, 2) the temperature-restricted kyanite- and staurolite-stable field, or 3) the kyanite-stable field (Figure 5a). Although the kyanite+staurolite stable field directly represents the peak assemblage of the major phases, the narrow temperature range in P - T space is at odds with the widespread occurrence of this assemblage in metamorphic terrains (Pattison & Spear, 2018). This discrepancy likely arises from the influence of sluggish reaction kinetics that yield the metastable persistence staurolite, or the minimal free energy difference between staurolite and kyanite nucleation. This latter option means kyanite may form earlier (Pattison & Spear, 2018), or staurolite may form later than that predicted by the thermodynamic models. In ICSV13, the consistency of microstructure, inclusion suite, and inclusion trail between kyanite and staurolite is suggestive of similar timing and conditions of growth. Given that nearby assemblages are predominantly kyanite-bearing rather than kyanite+staurolite-bearing (Cawood *et al.*, 2024), the staurolite-bearing fields are disregarded for this case. Therefore, the kyanite-bearing field on Figure 5a is chosen as the best representation of the peak field.

529 The peak assemblage field shows a wide P - T range over which the given rock composition
530 may have equilibrated. Temperature ranges between ~ 575 – 700 °C and pressure is poorly con-
531 strained owing to the dependence on the Ti-oxide phases to define the phase boundaries, which
532 are avoided here as a primary P - T constraint (e.g., Starr *et al.*, 2020). Consequently, the broad
533 range provided by the peak field in this sample is well suited to applying the workflow to further
534 constrain the conditions of metamorphism. Using the Ti-in-biotite geothermometer calibration
535 of Henry *et al.* (2005), the temperature of metamorphism is estimated at 590 ± 24 °C, whereas
536 pressure, determined using the avP function of THERMOCALC (Powell & Holland, 1994) at
537 the matching temperature, is constrained to 9.3 ± 0.8 kbar (1σ), in agreement with the peak
538 assemblage field (Figure 5a).

539 4.2.2 Grid-search inversion and uncertainty analysis

540 The inversion workflow was performed on a 100×100 grid in P - T space from 400 – 700 °C
541 and 5 – 13 kbar with 1000 random sets of samples drawn from the mineral measurement data
542 using bootstrap re-sampling assuming a normal distribution. The salient standard deviations
543 and mean values for each mineral measurement variable are provided in Table 4. Based on the
544 interpreted peak mineral assemblage, the variables used for this analysis are X_{Gr} , X_{Sps} , X_{Prp} ,
545 X_{Mg} of garnet, Si, Ti, and X_{Mg} of biotite, Si, X_{Pa} , and X_{Cel} of muscovite, and X_{Ab} of plagioclase
546 (see Table 1 for definitions). The P - T results are reported as median and IQR.

547 For the selected variables, the isopleth fields defined by the 2σ population show broad
548 agreement between the variables (Figure 4a). The inversion found a best-fit solution of 576 °C
549 (IQR 573 – 582 °C) and 9.53 kbar (IQR 9.28 – 9.85 kbar; Figure 5c). This result and associated
550 uncertainty show excellent agreement with the independent avP and Ti-in-biotite results (ther-
551 mobarometer intersection) and the peak assemblage field (Figure 5b). The residuals for each
552 variable, showing the relationship between the normalised distribution of the observed data and
553 the best-fit model prediction, are shown in Figure 4d. Each of the mineral measurement vari-
554 ables shows strong agreement with the best-fit model, except X_{Mg} in biotite that was removed
555 due to poor fit ($X_{\text{total}} > 1$), in addition X_{Cel} was also removed due to poor fit coupled with
556 a sensitivity in excess of 2% of the mean. Both the temperature and pressure best-fit solution
557 are particularly sensitive to the garnet composition. For example, the system has a ΔP of 0.76
558 kbar and 0.38 kbar for X_{Sps} and X_{Gr} , respectively (Table 5).

559 4.3 ICSV117

560 4.3.1 *Conventional methods of analysis*

561 For the inferred equilibrium assemblage of hornblende-biotite-plagioclase-quartz-ilmenite-
562 H₂O, a broad P - T zone of modeled peak assemblages show partial matches. Petrographic
563 observations show that titanite growth dominantly post-dates ilmenite growth, however it is
564 unclear whether titanite represents peak conditions or growth during decompression from peak
565 conditions. In either scenario, the relationship of Ti-oxide phases is not reproduced in a clockwise
566 P - T path on the modeled diagram, therefore as applied for ICSV13, the Ti-stability fields are
567 not prioritised. Furthermore, the presence or absence of clinopyroxene is not deemed relevant
568 to phase boundaries in clinopyroxene-absent assemblages owing to its predicted overstability
569 in modeled metabasic systems (Forshaw *et al.*, 2019). Therefore, the high-pressure boundary
570 of the matching peak assemblage fields is delimited by garnet and at lower temperatures by
571 epidote stability. This zone extends for a greater range of temperatures than modeled (550–750
572 °C) and to lower pressures than modeled, but extends up to ~10.0 kbar (Figure 5f). Using
573 the Hornblende-Plagioclase exchange geothermometer calibration of Holland & Blundy (1994),
574 the temperature of metamorphism is constrained to 644 ± 40 °C, and the pressure, using the
575 avP function of THERMOCALC at the matching temperature, to a value of 13.6 ± 2.4 kbar
576 (1 σ). The thermobarometer intersection shows no overlap with the peak assemblage field,
577 temperatures are in agreement but pressures are in excess of ~10.0 kbar for avP results (Figure
578 5f).

579 4.3.2 *Grid-search inversion and uncertainty analysis*

580 The inversion workflow was performed on a 100 x 100 grid in P - T space from 550–750 °C and
581 6–14 kbar with 1000 random sets of samples drawn from the mineral measurement data using
582 bootstrap re-sampling assuming a normal distribution. The salient standard deviations and
583 mean values for each observational variable are provided in Table 4. Based on the interpreted
584 peak mineral assemblage, the variables used for this analysis include those found in pelitic
585 compositions (Ti, Si and X_{Mg} of biotite and X_{Ab}) in addition to Ts (tschermakite, Al(T)-Na(A)-
586 K(A)), Ed (edenite, Na(A)+K(A)), Gln (glaucophane, Na(M4)) vectors and Ti in amphibole
587 (see Table 1 for full metabasic variables). The use of vectors in amphibole was deemed essential
588 to reduce dependency of the result on overestimated (Al and A-site Na) or underestimated (Si,

589 Ca and A-site K) cations (Forshaw *et al.*, 2019).

590 The mineral compositional variables produce a median best-fit solution at 669 °C (IQR =
591 659–677 °C) and 11.82 kbar (IQR = 11.66–11.98 kbar; Figure 5g, h; Table 6), in agreement
592 with the thermobarometer intersection but not the peak assemblage field. Si in biotite and the
593 Ed vector were sequentially removed to produce an X_{total} below 1 (Table 6). The pressure of
594 the result is largely defined by the shallow slope of X_{Mg} , X_{Ab} , Gln vector, (Figure 5j), and
595 was particularly sensitive to the values of the Gln vector and Ti in biotite, with ΔP values
596 of 0.45 and 0.42 kbar, respectively. Although the Ti in biotite variable is relatively pressure
597 insensitive, the value determines the intersection point with variables which are more pressure
598 sensitive (i.e., sloping P - T gradients), and therefore has an important role to play in determining
599 pressure (Figure 5j).

600 The calculated P - T result lies within a garnet-bearing field, despite the absence of garnet
601 in the observed assemblage (Figure 5g). As previously outlined, the domain in which the misfit
602 function is likely to find a best-fit solution reflects the phases presence or absence of phases
603 used in the selected variables for the inversion. In this case, there is no penalty for garnet
604 being predicted despite its absence in the interpreted equilibrium assemblage. Fixing the peak
605 field would likely lead to little or no agreement between the selected variables within that do-
606 main (Figure 5j). Three possible explanations for this discrepancy are considered. (1) The
607 analyzed rock volume may include modally minor garnet. The lack of garnet observed within
608 three-different observational scales (outcrop, hand sample, and thin-section scale), means this
609 scenario is disregarded. (2) Disequilibrium processes: petrographic evidence shows that for the
610 major assemblage chemical and textural equilibrium is dominant over the thin section-scale.
611 Furthermore, the narrow uncertainty range of the best-fit solution and the lack of a multi-modal
612 solution distribution (Figure 5h, i) suggest the effect of disequilibrium is not significant across
613 the analysed volumes. (3) Inaccuracies in the a - X solution models: for metabasic compositions
614 there is negligible reported difference in predicted and observed modal abundances for garnet
615 (Forshaw *et al.*, 2019), thereby making it unlikely that garnet is simply overstabilised for the
616 modeled composition. Instead, the more significant issue likely arises from the errors in element
617 partitioning between phases and the incorrect prediction of substitution vectors in the formula-
618 tion of the a - X models. These decisions lead to mismatches between predicted and observed
619 values for amphibole and clinopyroxene. This inevitably impacts the whole assemblage, and the

effect becomes more pronounced with higher modal abundances of these minerals. Given that amphibole is the modally dominant mineral in ICSV117, these mismatches create a cascading effect, impacting the predicted amphibole substitution vectors and other phase variables, such as Na content in plagioclase, both of which provide key constraints on the P of the best-fit solution. This also explains the overlap of the best-fit result with the independent thermobarometer intersection, as well as the deviation of the calculated P - T result from the peak assemblage field. In this case, the latter scenario is favoured.

5 SYNTHETICS

The grid-search inversion and bootstrap resampling is now employed on the worldwide median pelite composition of Forshaw & Pattison (2023) to provide a generalized estimate of uncertainty across sub-solidus P - T space. In an inversion method such as this—assuming the method itself is inerrant and there is no model uncertainty—uncertainties in the inverse solution arise from the uncertainties in input data and/or the forward model predictions. To explore these uncertainties, we follow the framework outlined in Figure 1 and consider three different sources of observational uncertainty, each influencing the inverse solution in a distinct way. (1) Mineral Measurement Uncertainty (MMU)—uncertainty in the input data used to constrain the inverse solution (phase compositions and/or phase modal volumes). Here, the data is varied while the forward model remains fixed. (2) Bulk Composition Uncertainty (BCU)—uncertainty in the forward model predictions, propagated from uncertainty in the modeled bulk composition. In this case, the forward model is varied while the input data remains fixed. (3) Observational Uncertainty (OU)—the combined effects of both MMU and BCU , where both the input data and forward model predictions are varied simultaneously. To evaluate these uncertainties, the inverse solution is constrained using three different types of input data (a) mineral compositions only, (b) mineral modal volumes only, and (c) a combination of mineral compositions and modal volumes. This framework, allows us to assess how the impact of each uncertainty source varies across P - T space and in relationship to the different types of input data.

The variables of interest include X_{Gr} , X_{Prp} and X_{Sps} of garnet, Ti, Si and X_{Mg} of biotite, X_{Cel} , X_{Pa} and Si of muscovite, X_{Ab} of plagioclase, X_{San} of K-feldspar, X_{Mg} of chlorite, X_{Mg} of staurolite, X_{Mg} of cordierite, and X_{Fe} of epidote (see Table 1 for definitions). The modal volume of each of the aforementioned phases is also used for this analysis, as well as the modal

649 volume of the three Al_2SiO_5 polymorphs, quartz, and titanite. All uncertainty measurements
650 are calculated as one standard deviation. Where uncertainties are given for a range of pressure
651 or temperature conditions, these are median values of the distribution of standard deviation
652 measurements.

653 For each setup, forward models were created between 350–750 °C and 0.001–13 kbar for
654 the worldwide median pelite composition in THERIAK-DOMINO (de Capitani & Brown, 1987;
655 de Capitani & Petrakakis, 2010). This analysis does not consider the impact of varying model
656 uncertainty. Instead, the analysis is performed using a fixed set of models, the details of which
657 are outlined in the Supplementary Text. In each case the system was saturated with 30 mol % of
658 pure H_2O . To ensure the uncertainty of P - T points around the boundary of the model was not
659 artificially decreased, the results were only considered between 1–12 kbar and 400–700 °C. The
660 solution uncertainties for each uncertainty sources are displayed in Figures 6,7, and 8, respec-
661 tively, with the biotite-, garnet-, and porphyroblast(cordierite/andalusite/staurolite/kyanite)-in
662 lines overlaid on each plot. The calculation outputs used in each figures, and referenced in the
663 text, are located in the Supplementary material (Table S5).

664 5.1 The impact of mineral measurement uncertainty, *MMU*

665 For this analysis, the bulk-rock $X_{\text{Fe}^{3+}}$ was fixed at 0.1, and the forward model was created
666 over a 100 x 100 grid. Two-hundred synthetic mineral measurement datasets for each point on
667 the P - T grid were constructed by bootstrap resampling. The value of each variable in these
668 datasets was selected by repeated sampling of a normal distribution using the mean of the
669 predicted data and a standard deviation equivalent to 10 % of the mean. The value of 10 %
670 (for 1 σ) was chosen following the highest uncertainty value estimated by Palin *et al.* (2016).
671 The best-fit P - T solution was found for each of the 200 synthetic datasets generated at each
672 P - T point. The spread in these 200 best-fit solutions, measured using the standard deviation,
673 quantifies the uncertainty at each P - T point in the grid. The solution uncertainty for each
674 variable type is shown in Figure 6a–f. The median uncertainty over the modeled P - T space is
675 shown in Figure 6g, h.

676 Using composition variables only, the temperature uncertainty is 9 °C, compared to 12 °C
677 for modal volume variables only (Figure 6g). When these two variable types are combined, the
678 uncertainty drops to 6 °C (Figure 6g). This demonstrates the importance of determinacy: a

greater number of variables often leads to a lower solution uncertainty. The same is true for pressure uncertainty: 0.7 kbar and 0.4 kbar using the composition and modal volume datasets, respectively, which decreases to a 0.2 kbar uncertainty when the composition and modal volume datasets are combined (Figure 6h). The uncertainty is significantly controlled by the phase assemblage. For example, the temperature uncertainty, using composition and modal volume variables together, decreases from 13 °C to 3 °C where garnet is present in the assemblage.

5.2 The impact of bulk composition uncertainty, *BCU*

To assess the impact of *BCU*, a Monte-Carlo simulation was performed to create 100 random variations of the worldwide median pelite composition. Each oxide was varied at the same time and then re-normalized. The weight percentage of each oxide and the bulk $X_{\text{Fe}^{3+}}$ was allowed to vary within an amount characteristic of a natural assemblage following the example used in Palin *et al.* (2016) (see Table 7). In this scenario, the bulk composition is treated as if it were a total bulk derived via XRF. The reasons why it may not be applicable to other methods of deriving bulk composition is covered in Section 6.1.1.

Forward models were created for each of the 100 bulk compositions in a 75 x 75 grid. The range of these models therefore represent the uncertainty in the forward model predicted data from the variation of the bulk composition. The “true” bulk composition is assumed to lie within this model distribution. The synthetic input data, defined for the previously outlined variables, was constructed at each *P-T* point within the 75 x 75 grid using the recorded composition of the worldwide median pelite. The synthetic data were then passed through a grid-search routine for each of the 100 forward models, and the spread of the best-fit *P-T* solutions was analysed. The solution uncertainty for each variable type is shown in Figure 7a–f and the median uncertainty over the modeled *P-T* space is shown in Figure 7g, h.

The difference between the composition variables and the modal volume variables are larger for *BCU* than for *MMU*. For temperature, the use of composition variables results in an uncertainty of 11 °C, whereas the modal volume variables result in an uncertainty of 35 °C (Figure 7g). This pattern is also observed in the pressure domain, with an increase in from 0.6 kbar to 1.4 kbar when modal volume variables are used (Figure 7h). The *P-T* uncertainty derived from *BCU*, using composition and modal volume variables together, is 19 °C and 0.9 kbar.

708 5.3 The impact of observational uncertainty, *OU*

709 The impact of *OU* (which comprises both *BCU* and *MMU*) was examined using a combined
710 approach of the sample bootstrapping and the Monte-Carlo variation in bulk composition. Two-
711 hundred synthetic observation datasets for each point on the *P-T* grid were constructed for each
712 variable via repeated sampling of a normal distribution with a standard deviation set to 10 %
713 of the mean. The forward modeled data from the worldwide median pelite served as the sample
714 mean for the resampling distribution. A bulk composition was then randomly selected from the
715 100 available forward models for each of the 200 bootstrap resamples. A grid-search inversion
716 was then applied to calculate the best-fit solution for each of the 200 re-sampled datasets at
717 each *P-T* point. The spread of the best-fit solutions therefore represents the *P-T* uncertainty
718 introduced by both *MMU* and *BCU*. The solution uncertainty for each variable type is shown
719 in Figure 8a–f and the median uncertainty over the modeled *P-T* space is shown in Figure 8g,
720 h.

721 Using composition variables produces a lower temperature and pressure uncertainty (16
722 °C, 0.7 kbar) than for modal volume variables alone (36 °C, 1.4 kbar; Figure 8g, h). The
723 temperature uncertainty using composition and modal volume variables together is 21 °C and
724 the pressure uncertainty is 1.0 kbar (Figure 8g, h). When using the composition and the modal
725 volume variables together, the addition of biotite to the stable assemblage increases pressure
726 and temperature uncertainty by 27 % and 44 % respectively. The presence of garnet in the
727 equilibrium phase assemblage also has a significant impact on the temperature uncertainty (28
728 °C garnet absent, 14 °C garnet present) but a negligible impact on pressure uncertainty (0.9
729 kbar garnet absent, 1.0 kbar garnet present).

730 5.4 The impact of uncertainty source and variable type across *P-T* space

731 The results from the analyses in Section 5.1, Section 5.2, and Section 5.3 have been binned
732 into different domains (Figure 9; Carmichael, 1978; Pattison & Tracy, 1991) to compare the
733 impact of the uncertainty source and the variable type on the solution uncertainty across *P-T*
734 space. The “chl/bt”, “grt”, “porph”, and “sil” denote metamorphic zones—respectively, the
735 chlorite/biotite zone (temperatures up to 425 °C), garnet zone (425–550 °C), porphyroblast
736 zone (comprising cordierite/andalusite/staurolite/kyanite, 550–625 °C), and sillimanite zone
737 (625–700 °C). In contrast, “crd”, “st”, and “ky” define the pressure-dependent facies series:

738 the cordierite series (cordierite–andalusite–sillimanite, 0–3.5 kbar), the staurolite series (staurolite–andalusite–sillimanite, 3.5–6.5 kbar), and the kyanite series (staurolite–kyanite–sillimanite, 739 above 6.5 kbar). The distribution of these metamorphic zones and facies series is illustrated 740 in Figure S3. The temperature and pressure ranges do not strictly denote the stability of the 741 aforementioned minerals, and should therefore be used solely to inform the broader changes in 742 metamorphic grade. 743

744 Using composition variables, the uncertainty in both temperature and pressure derived from 745 *OU* decreases from the biotite zone to the porphyroblast zone and then minorly increases from 746 the porphyroblast zone into the sillimanite zone (Figure 9a, d). For example, the pressure 747 uncertainty shows the following trend: 1.0 kbar (biotite zone), 0.8 kbar (garnet zone), 0.7 kbar 748 (porphyroblast zone) and 0.8 kbar (sillimanite zone). This pattern is mirrored when using 749 *MMU* and *BCU* separately, with the *BCU* producing the higher uncertainty of the two. This 750 is notable in the chlorite/biotite zone, where accounting for *BCU* produces uncertainties of 751 21 °C and 0.9 kbar, compared to *MMU*, which produces an uncertainties of 14 °C and 0.6 752 kbar. For *OU*, temperature uncertainty decreases with increasing pressure conditions from the 753 cordierite series to the kyanite series. This is largely driven by effects of *MMU*, for which the 754 temperature uncertainty decreases significantly between the two series (21 °C, 14 °C, and 5 °C, 755 respectively) whereas the temperature uncertainty attributed to *BCU* is largely constant. For 756 *OU*, pressure uncertainty varies between 0.7–0.8 kbar. From lower to higher facies series, the 757 pressure uncertainty derived from *MMU* decreases, but increases for *BCU* .

758 When only using modal volume variables, the most notable trend is the low solution un- 759 certainties derived from *MMU*, relative to the higher uncertainties derived when applying *BCU* 760 (Figure 9b, e). This discrepancy is present across all metamorphic zones and facies series. For 761 example, in the garnet zone the uncertainty derived from *MMU* is 8 °C and 0.5 kbar compared 762 to the uncertainty from *BCU* of 37 °C and 2.0 kbar. In the kyanite series, the uncertainty for 763 the *MMU* approach is 4 °C and 0.2 kbar compared to the uncertainty for the *BCU* approach of 764 26 °C and 1.3 kbar. For *BCU*, the calculated temperature and pressure uncertainty decreases 765 with increasing metamorphic grade and facies series. The uncertainty in the biotite zone is 46 766 °C and 2.1 kbar compared to 15 °C and 0.9 kbar in the sillimanite zone. The exception to this 767 is the transition from the cordierite series to the kyanite series.

768 When the mineral composition and modal volume variables are used together, the calculated

uncertainties show a similar pattern to that of the modal volume-only results (Figure 9c, f), suggesting uncertainty in modal volumes has the largest impact on the uncertainty in estimated P - T conditions. *BCU* produces decreasing pressure and temperature uncertainties moving from lower to higher metamorphic zone and facies series. This is also observed for uncertainties derived from *OU*: in the biotite zone, the uncertainty is 30 °C and 1.8 kbar, whereas the porphyroblast zone has an uncertainty of 16 °C and 0.8 kbar. An exception to this pattern is the facies series, which shows the expected decrease in temperature uncertainty but a modest increase in pressure uncertainty from lower to higher facies. When accounting for *OU*, the cordierite series has an uncertainty of 29 °C and 0.9 kbar, whereas the kyanite series has an uncertainty of 16 °C and 1.0 kbar.

It is also worth noting the relative magnitude of the uncertainties when using composition variables compared to using modal volume variables. Each metamorphic zone and facies series shows an increased uncertainty when using modal volume variables in comparison to composition variables and is irrelevant of the uncertainties applied to the inversion calculation (*MMU*, *BCU*, or *OU*). In the garnet zone, the *OU* when using composition variables is 16 °C and 0.7 kbar (Figure 9a, d) in contrast to 38 °C and 2.0 kbar when modal volume variables are used (Figure 9b, e). In the porphyroblast zone, the uncertainty is 14 °C and 0.7 kbar when using composition variables, in comparison to 28 °C and 1.2 kbar when using modal volume variables. In the cordierite series, there is an uncertainty of 24 °C and 0.7 kbar when using composition variables, compared to 49 °C and 1.3 kbar when using modal volume variables. Across the total modeled P - T space modal volume variables approximately double the uncertainty of composition variables (220 % higher T uncertainty and 185 % higher P uncertainty; Figure 8).

The impact of *MMU*, *BCU*, and *OU* for temperature and pressure uncertainties has also been quantified for each individual composition and modal volume variable (Figure 10). The resulting uncertainties vary quite significantly between those associated with different phases and even between different composition variables from the same phase. For example, the behaviour of the four garnet variables (X_{Alm} , X_{Prp} , X_{Grs} , X_{Sps}) is relatively varied. X_{Prp} shows the lowest temperature uncertainty of the four, with a *OU* temperature uncertainty of 32 °C. X_{Alm} is particularly sensitive to *MMU* relative to *BCU*, with temperature uncertainties of 81 °C and 60 °C, respectively. Given almandine is commonly the largest mole fraction in a constant-sum composition, variation from other phase components more strongly influence the absolute value

(Kohn & Spear, 1991b; Waters, 2019). For the composition variables, uncertainties from *MMU* are slightly higher than those derived from *BCU*. For example, *MMU* for X_{Ab} in plagioclase results in a temperature uncertainty of 98 °C, compared to 90 °C for *BCU*. Indeed, some variables show a significant lack of sensitivity to *BCU*. For example, Ti in biotite has a temperature uncertainty of only 17 °C for *BCU*. However, some are notably more sensitive, for example X_{Mg} in biotite has a temperature uncertainty of 69 °C. Finally, the modal volume variables for the Al-rich phases (staurolite, kyanite, sillimanite, and andalusite) can be used to constrain the calculated temperature and pressure conditions with low uncertainties across any uncertainty approach applied to the inversion. However, it should be noted that the low uncertainty displayed by kyanite (20 °C) is likely an artifact of the model limits and/or nature of the worldwide pelite composition, for which kyanite only joins the assemblage at high *P-T* conditions. The modal volume of cordierite and K-feldspar are also notable for their low pressure uncertainties of 1.0 and 0.8 kbar (*OU*), yet higher temperature uncertainties of 112 and 70 °C (*OU*), respectively.

5.5 A comparison between uncertainty sources along a geotherm

The effects of *MMU*, *BCU*, and *OU* were also examined at 75 points along a typical continental-crust geotherm from Copley & Weller (2022). The distribution of this geotherm is shown in Figure S4. Bootstrap re-sampling (*MMU*) was performed on mineral measurements at 10 % and 20 % of the mean values predicted by the forward models. The *BCU* analysis was performed using the Monte-Carlo approach as outlined in Section 5.2, and the *OU* analysis was performed combining the above approaches, using bootstrapping at 10 % of the mean. The results of this analysis are presented in Figure 11.

For the composition variables, the *OU* is dominantly controlled by the effects of the *BCU* (Figure 11a, d). For example, before biotite becomes part of the stable assemblage, the temperature uncertainty derived from *BCU* exceeds that from the 10 % bootstrapped *MMU*. This is also consistent after garnet joins the assemblage, but prior to growth of staurolite. At chlorite-grade conditions, pressure uncertainty derived from *MMU* exceeds that from *BCU*. However, once biotite joins the stable assemblage, the pressure uncertainty derived from *BCU* is consistently greater than that from the 10 % bootstrapped *MMU*. Notably, *P-T* uncertainties from the 20 % bootstrapped *MMU* exceed those from *OU* at all points along the geotherm, suggesting that when relying solely on compositional variables, a high bootstrap threshold may be sufficient to estimate the “total” *OU* without requiring Monte Carlo bulk composition analysis.

831 When using modal volume variables alone, the P and T uncertainties derived from BCU are
832 consistently in excess of the uncertainty from the 10 % bootstrapped MMU , and near consistently
833 greater than the 20 % bootstrapped MMU (Figure 11b, e). The bootstrapping on mineral
834 measurements at 20 % is therefore unable to account for uncertainty in the bulk composition.
835 This is particularly true near phase boundaries (e.g., biotite-in and staurolite-in), where the P
836 and T uncertainties derived from the MMU are significantly lower than that derived from the
837 BCU .

838 Where both mineral composition and volume variables are used, the trend of P and T un-
839 certainties derived from MMU and BCU is often directly opposing across the modeled geotherm
840 (Figure 11c, f). The combined OU more closely follows the trend of the BCU , again suggest-
841 ing the overall uncertainty stemming from the observations is most strongly impacted by BCU
842 rather than BCU . P and T uncertainties shows a marked increase at biotite-in with another
843 marked decrease at garnet-in. The addition of staurolite results in a minor increase in temper-
844 ature uncertainty, but appears to stabilise pressure uncertainty as the geotherm progresses to
845 higher-grade conditions (Figure 11c, f). As in previous sections, the results demonstrate that
846 calculated uncertainties vary significantly across P - T space, as does the relative importance of
847 MMU and BCU .

6 DISCUSSION

848 The techniques used to examine the P - T evolution of metamorphic sequences have made
849 considerable advances over recent decades. Despite a long-standing appreciation of the im-
850 portance of uncertainty in P - T analyses (e.g., Hodges & McKenna, 1987; Powell & Holland,
851 1988, 1994; Kohn & Spear, 1991a, b; Worley & Powell, 2000; Powell & Holland, 2008; Palin
852 *et al.*, 2016), the majority of studies employ qualitative comparisons between predicted and ob-
853 served phase information without accounting for, or quantifying, uncertainty within the system.
854 Therefore, this discussion evaluates (1) the relative impact of different uncertainty sources and
855 variable types on inverse solution uncertainties, (2) explores systematic controls on uncertainty
856 in natural systems, (3) compares our results to previous uncertainty estimates, and (4) exam-
857 ines the benefits and limitations of the new grid-search inversion technique for metamorphic
858 studies.

6.1 Uncertainty estimates in pelitic systems

The data presented in this study demonstrate that both mineral measurement uncertainty and bulk composition uncertainty can have a significant impact on P - T estimates, and that the magnitude of the impact varies with P - T grade and the type of observational variables used in the inversion (mineral composition, mineral modal volume, or both).

6.1.1 The impact of uncertainty source

Bootstrapping of mineral measurements (mineral measurement uncertainty) at an appropriate percentage ($\sigma = \text{mean} \times \sim 20\%$) and using solely mineral composition variables will generally account for the total observational uncertainty (e.g., Figure 11a, d). However, when applying mineral measurement uncertainty using mineral modal volume variables the pressure and temperature uncertainties locally drop to zero or near-zero at phase boundaries (Figure 11b, c, e, f). These pressure and temperature uncertainties show that bulk composition uncertainty has a significant impact on pseudosection topology (e.g., Stüwe, 1997; Guevara & Caddick, 2016; Palin *et al.*, 2016; Lanari & Engi, 2017). Therefore, when using modal volume variables near phase stability boundaries, bulk composition uncertainty should be accounted for in order to constrain a solution uncertainty that characterizes the total observational uncertainty in the system.

It should be noted that the impact of the uncertainty in bulk composition depends on how the bulk composition was measured (e.g., total vs effective) and what type of variables are used for the inversion. The effective (also termed reactive) bulk composition can be calculated from the observed phase assemblage by using the measured oxide composition of each phase (X_{ij}) in equilibrium within the assemblage and the observed modal abundance of each phase (v_j ; Equation 8).

$$X_i^{bulk} = \sum_{j=1}^p X_{ij} \cdot v_j \quad (8)$$

Where X_i^{bulk} is the bulk composition of the rock, with a weight percent for each oxide (i). There are a total of p phases in the rock. Assuming that the phase compositions (X_{ij}) are well known, then the only source of uncertainty in the calculated bulk composition is the phase abundance (v_j). In this case, assuming an equilibrium scenario (a single P - T point) and

no model uncertainty, the uncertainty in the bulk composition has no impact on the predicted phase compositions and assemblages (see Model 2A in Lanari & Hermann, 2021). In this case, the use of phase compositions for the inversion are significantly preferred to phase abundance (modal volumes). However, if there is significant uncertainty in the observed phase composition, equilibrium assemblage, and/or thermodynamic models (as is likely when investigating a natural system), then this will propagate through to uncertainty in both the predicted phase modal volume and phase composition. In this case, including mineral modal volumes in conjunction with other variables may aid in stabilising the complex non-linear nature of P - T analysis. The scenario outlined here does not apply if P - T conditions change, as is the case for a pseudosection, as the position of many reactions is controlled by the effective bulk composition (Palin *et al.*, 2016; Lanari & Duesterhoeft, 2019). If the bulk composition has been derived by XRF (total bulk composition), it represents the overall oxide abundances measured independently from observed phase composition and modal volume. This is the type of bulk composition measurement simulated in Section 5.2 of this study, and was shown to have a clear impact on the uncertainty in the predicted composition and modal volumes of phases throughout P - T space.

6.1.2 *The impact of variable type*

Using mineral composition variables generally produces lower median pressure and temperature uncertainties than using modal volume variables (Figures 6, 7, and 8). Each mineral composition and modal volume variable shows distinct sensitivity to uncertainties in mineral measurements and bulk composition (Figure 10). Broadly mineral composition variables are notably less sensitive to bulk composition than mineral modal volumes or phase stability boundaries. This makes mineral composition variables valuable tools for calculating P - T estimates, providing constraints that are less dependent on one of the largest sources of uncertainty within modelling (bulk rock composition; Figure 10). For example, Ti in biotite is relatively insensitive to bulk composition uncertainty ($1\sigma = 17^\circ\text{C}$), which aligns with natural observations where systematic Ti variations correlate with metamorphic grade despite variation in bulk rock composition (Henry & Guidotti, 2002). However, a notable exception is that the X_{Mg} of biotite ($1\sigma = 69^\circ\text{C}$, from bulk composition uncertainty). Therefore, although the calibration of the Ti- X_{Mg} relationship is based on a natural dataset (Henry *et al.*, 2005), and although a - X models may not perfectly reproduce the natural system (e.g., Guevara & Caddick, 2016; Kendrick & Indares, 2018; Waters, 2019; Gervais & Trapy, 2021), the variation of calculated temperatures from the

917 thermometer will likely reflect not only metamorphic grade but also the significant influence of
918 bulk composition.

919 Given the differing P - T uncertainty associated with the variables it may be tempting to
920 select those that produce the most certain solution. The use of pseudosection stability fields
921 combined with preferential isopleth or isomodes can offer impressively precise results P - T es-
922 timates (Figure 2). However, in order to provide an estimate of both the P - T conditions and
923 associated uncertainty that is representative of the modeled system, the widest and most diverse
924 possible range of robust variables should be incorporated during the inversion (whilst allowing
925 for a degree of freedom). Care must be taken to exclude variables with significant model error,
926 as these may degrade the result (Powell & Holland, 2008), though as the L1-norm function is
927 robust to outliers (Claerbout & Muir, 1973), the impact of this should be lessened. This ap-
928 proach enables an assessment of the overall model performance, which may provide insights into
929 other characteristics of the system such as the degree of equilibrium.

930 **6.1.3 The impact of metamorphic grade**

931 The “total” observational uncertainty (derived from OU using both mineral composition
932 and modal volume variables) was found to vary across P - T space (Table 8), with a particular
933 difference between the lower-temperature biotite and garnet zone ($1\sigma = 25$ – 30 °C, 1.2 – 1.8 kbar)
934 and the higher-temperature porphyroblast and sillimanite zone ($1\sigma = 16$ °C, 0.8 kbar). The
935 lowest-grade conditions therefore exhibit approximately double the uncertainty in P - T compared
936 to the highest-grade conditions. This pattern is partly reflected across the facies series, with
937 the highest-temperature uncertainty found at the lowest-pressure cordierite series ($1\sigma = 29$
938 °C), and lowest-temperature uncertainty in the highest-pressure kyanite series ($1\sigma = 16$ °C),
939 whereas the the pressure uncertainty remains nearly constant across all facies series ($1\sigma = 0.9$ –
940 1.1 kbar). The higher uncertainty at lower grades is predominantly caused by the impact of bulk
941 composition uncertainty on the inversion of modal volume variables (Figure 9b, e). This result,
942 is perhaps unsurprising given low grades are dominated by hydrous sheet silicates with broad
943 compositional ranges, fewer assemblage changes over small P - T spaces, and a lack of aluminous
944 porphyroblasts.

945 **6.1.4 *Tectonometamorphic controls on uncertainty in natural systems***

946 The synthetic uncertainty analysis performed in this study used the median worldwide pelite
947 composition from Forshaw & Pattison (2023), which represents a compilation of 5729 pelite
948 compositions from 11 different orogens or regions. Such a broad dataset provides generalised
949 insights into the metamorphic reactions and processes operating in pelitic systems. However,
950 it does not fully account for uncertainties that may systematically vary specific to changing
951 tectonometamorphic environments in natural systems. Different tectonic settings impart sys-
952 tematic compositional differences to deposited sedimentary units, which can be discriminated
953 using major-element geochemical proxies (e.g., Bhatia, 1985; Roser & Korsch, 1988; Verma &
954 Armstrong-Altrin, 2016). In addition, the degree of sediment reworking can impact composi-
955 tions systematically (e.g., McLennan *et al.*, 1993). Upon metamorphism, these compositional
956 differences influence the metamorphic equilibria, thereby affecting the observed mineral assem-
957 blages, phase proportions, and compositions within the resulting metamorphic sequence (Bucher
958 & Frey, 1994). For example, mature pelites, which are often depleted in plagioclase, can ex-
959 hibit large pressure uncertainties due to the loss of key barometric equilibria. Consequently,
960 different depositional environments and their resulting metamorphic sequence may inherently
961 exhibit different levels of uncertainty during petrological investigation (e.g., Caddick & Thomp-
962 son, 2008). Furthermore, tectonometamorphic environments differ in heat sources, radiogenic
963 heating levels, and rates of crustal thickening or erosion (Waters & Lovegrove, 2002; Copley &
964 Weller, 2022) which may influence the degree to which reactions occur at or near-equilibrium
965 conditions. Prograde metamorphism is governed by heating rates, with regional metamorphism
966 typically occurring near equilibrium conditions (e.g., Yardley, 1977), whereas contact metamor-
967 phism often preserves evidence of disequilibrium processes (e.g., Hollister, 1969; Voll *et al.*, 1991;
968 Wheeler *et al.*, 2004). The scale and effect of such processes vary considerably across individual
969 metamorphic sequences and are not quantifiable in a generalised sense. Given these consider-
970 ations, the synthetic uncertainty values presented in this study should be considered more as
971 guidelines than actual rules when assessing real rock systems.

972 **6.1.5 *Comparison with prior uncertainty estimates***

973 The uncertainty estimates reported in this study differ from those reported in previous stud-
974 ies in that they are separated as a function of metamorphic zone and facies series, emphasising
975 the impact of the changing assemblage (i.e., the phases present or absent). Previous studies have

976 reported various estimates of system uncertainty for conventional thermobarometry: ± 100 °C
977 and \pm several kbar (geological uncertainty, analytical uncertainty, and thermobarometer cali-
978 bration error; Hodges & McKenna, 1987); ± 0.60 – 3.25 kbar (geological uncertainty, analytical
979 uncertainty, and thermobarometer calibration error; 1σ ; Kohn & Spear, 1991b); $> \pm 50$ °C and
980 $> \pm 1$ kbar (2σ ; Powell & Holland, 2008), $> \pm 50$ °C and $> \pm 1$ kbar (Spear *et al.*, 2016); and
981 for phase equilibrium modelling $\pm \sim 1$ kbar (geological uncertainty, 20 % variation from mean,
982 2σ ; Palin *et al.*, 2016). This study reports an estimate for median observational uncertainty
983 (Figure 1) in subsolidus pelitic systems of 22 °C and 1.0 kbar at the 1σ level (10 % variation
984 from mean, Table 8). This is equivalent to 44 °C and 2.0 kbar at 2σ level (thereby 20 %
985 variation from the mean). This uncertainty is even higher where only modal volume variables
986 are considered, $1 \sigma = 36$ °C and 1.4 kbar ($2 \sigma = 72$ °C, 2.9 kbar).

987 6.2 Quantitative petrological modelling

988 6.2.1 Comparison to other quantitative workflows

989 Using petrological data to quantitatively invert for pressure and temperature is well estab-
990 lished. The avPT function of THERMOCALC (Powell & Holland, 1994) uses the activities of
991 phases involved in balanced independent chemical reactions from an internally consistent ther-
992 modynamic dataset to calculate the temperature and/or pressure. An iterative, least-squares
993 inversion is used to find the optimal P - T condition which maximises the consistency between
994 each independent chemical reaction involved within the inversion (Powell & Holland, 1994).
995 The same approach applies for avP and avT calculations, although these are calculated directly
996 without iteration (Powell & Holland, 1988). This approach calculates “predictive” uncertainties
997 (specifically those stemming from model uncertainty), in contrast to observational uncertainties
998 considered in the inversion method present in this study (Figure 1). TWEEQU (Thermobarome-
999 try With Estimation of EQUilibration state) follows a similar multi-equilibrium approach, calcu-
1000 lating all possible equilibria implied by selected phase components from an internally consistent
1001 thermodynamic database (Berman, 1991). The subsequent TWQ software (Berman, 2007), in-
1002 troduced a refinement by prioritizing an independent set of equilibria considered more robust,
1003 particularly those directly constrained by experimental data. While these methods are powerful
1004 and have been widely used, they remain independent from phase equilibrium modelling.

1005 Most recently, Bingo-Antidote uses the forward models calculated by a Gibbs Free Energy

Minimizer to perform inversions (Duesterhoeft & Lanari, 2020). Bingo-Antidote performs a global optimization of P and T as a function of the observed phase assemblage, mineral modes, and mineral composition. Bingo-Antidote incorporates all this information into a “global evaluation criterion” (Q_{total}). This method is particularly powerful due to its integration with XMapTools (Lanari *et al.*, 2019) and thus its ability to link directly to compositional phase maps, and examine the impact of local bulk composition variation on resulting P - T estimates. Some key differences between Bingo-Antidote and the new workflow proposed here are discussed in the Supplementary Text. Most notably, Bingo-Antidote and this workflow treat uncertainty estimates quite differently. Bingo-Antidote incorporates measurement uncertainties into its definition of its objective function, in a similar way to the chi-squared objective function. As such, lower values of Q_{total} indicate that the inversion is closer to the mean observed value for any given data variable. The uncertainty estimate provided in Bingo-Antidote is the area in P - T space with a Q_{total} score within 2 % of the maximum Q_{total} value. This can be thought of the goodness-of-fit error, which quantifies how well different potential solutions describe the mean value for each variable. However, this approach does not consider how the P - T solution might change as a result of uncertainty in the measurements or the impact of uncertainty in the forward models. In contrast, our new workflow uses bootstrap resampling for uncertainty propagation, showing how observational uncertainties affect the distribution of possible P - T solutions.

6.2.2 Advantages and limitations of the new workflow

Grid-search inversion The grid-search inversion offers a systematic approach to identify the global minimum of the misfit function and determine the best-fit solution within the selected model space. By discretizing P - T space into a grid of forward models and calculating the misfit at each grid point (Figure 3a), this method ensures the global minimum is located, provided the grid range and precision are appropriate. The grid-search is also advantageous because it is adaptable to various combinations of model parameters, such as T - X and P - X , making it applicable across a broad range of petrological modelling scenarios. Furthermore, the workflow is equally applicable to higher-dimensional analyses (e.g., P - T - X). However, the grid-search approach introduces computational challenges as the number of trial solutions increases exponentially with increasing dimensionality. Advances in forward modelling software (e.g., Riel *et al.*, 2022) have significantly reduced the computational time required for these calculations, thereby opening up the extension of this workflow to higher dimensions and reducing the need for assigning

1037 parameters a priori (e.g., $X_{\text{Fe}^{3+}}$, $a\text{H}_2\text{O}$).

1038 **Misfit/objective function** The workflow employs the L1-norm misfit function, a robust
1039 measure of fit that is widely used across scientific disciplines because of its resilience to outliers,
1040 outperforming L2-norm (least-squares) or chi-squared functions in this regard (Claerbout &
1041 Muir, 1973; Li *et al.*, 2015; Ibraheem *et al.*, 2021). This makes the method particularly well-
1042 suited for petrological systems where significant outliers are common.

1043 The inversion does not directly identify the stable phase assemblage, unless the variables are
1044 set to accommodate this. Rather, the misfit function seeks solutions in which all phases included
1045 in the selected variables are of the correct composition and/or modal abundance, thereby defined
1046 by where these phases are predicted to be stable. Therefore the boundaries of the result are
1047 inherently dependent on the variables employed in the inversion. The lack of strict relationship
1048 between the misfit function and a user-defined peak assemblage field has several benefits: (1) The
1049 assemblage field corresponding to a mineral assemblage in a pseudosection may be smaller than
1050 the estimated uncertainty (Powell & Holland, 2008; Waters, 2019); (2) field boundaries defined
1051 by small modal volume or accessory phases may not be reliable (Weller *et al.*, 2024); and (3)
1052 assemblage field boundaries, mineral mode contours, and mineral compositional isopleths show
1053 relatively decreasing uncertainties and increasing precision (Waters, 2019).

1054 The misfit function does not inherently penalize inversions using a small number of variables.
1055 Instead, the impact of the number of variables is best understood by analysing the standard
1056 error (SE). The number of variables will also have a significant impact on the P - T uncertainty
1057 derived from bootstrap resampling, discussed below. A notable feature of this workflow is its
1058 deliberate avoidance of variable weighting, such that all variables are treated as equally valid
1059 in the inversion. This approach is advantageous in scenarios where the relative importance of
1060 variables is difficult to determine or where weighting would introduce significant bias into the
1061 results.

1062 **Uncertainty analysis** Formal error propagation is generally unsuitable for non-linear prob-
1063 lems such as inverting for P - T conditions, because the combined effects of various random and
1064 systematic errors are impossible to calculate directly (Menke, 1984). Instead, Monte Carlo meth-
1065 ods, such as bootstrap resampling, are particularly well suited. The application of bootstrap
1066 resampling to the observed data allows users to estimate the uncertainty of the inverse solution

1067 (Figure 3b). It may also be used to identify any significant local minima that may provide
1068 alternative hypotheses and to evaluate the sensitivity of the final result to the different input
1069 variables (Figure 4e).

1070 Although the workflow incorporates multiple sources of uncertainty stemming from the
1071 observations, not all quantifiable and semi-quantifiable uncertainties are fully addressed (Figure
1072 1). Uncertainty in the parameters used during modelling and the underlying thermodynamic
1073 end-member datasets and a - X relations are not directly examined by bootstrap resampling
1074 and may unduly influence the forward modeled values. Nevertheless, the method inherently
1075 incorporates some of these uncertainties due to reliance on Monte Carlo-style methods (Figure 1).
1076 The impact of these uncertainties on the solution could be more directly analyzed by performing
1077 Monte-Carlo simulations of the forward problem with varying input parameters, solution models
1078 and databases.

7 CONCLUSIONS

1079 Accurately constraining the P - T history of metamorphic rocks is crucial for understanding
1080 a broad range of processes in both the solid and surficial Earth, including identifying geothermal
1081 gradients in the subsurface and sources of economically valuable raw materials (e.g., critical met-
1082 als), understanding climate and Earth system feedbacks, reconstructing the tectonometamorphic
1083 evolution of terrains, and informing broader geodynamic models. The ability to understand and
1084 quantify uncertainties in the calculation of P - T conditions is essential to ensuring that results
1085 can be interpreted within a defined confidence range. This is particularly important in scenarios
1086 where geological or petrological interpretations hinge on relatively small variations in pressure
1087 and/or temperature (e.g., Pattison & DeBuhr, 2015). Although many sources of uncertainty in
1088 phase equilibrium modelling cannot be propagated or are difficult to quantify, for those that can
1089 be, there should be an attempt to do so (Powell & Holland, 2008). The key conclusions of this
1090 study are:

- 1091 1. The new workflow, LinaForma, provides quantitative constraints on optimal P - T con-
1092 ditions and associated uncertainties for a given rock system. The technique identifies
1093 the best-fit solution by comparing observed data, such as mineral compositions and/or
1094 modal volumes, with forward model predictions across a user-defined P - T grid. Boot-
1095 strap resampling (repeated sampling with replacement) quantifies the uncertainty of the

inverse solution and assesses its sensitivity to input variable uncertainty. Three diagnostic metrics—quality of data fit, variable sensitivity, and standard error—are incorporated to validate and refine the results.

2. Application to natural samples demonstrates that peak P - T conditions and uncertainty estimates for both pelitic and metabasic compositions align with classical thermobarometric methods. Local discrepancies help assess model limitations.

3. In a synthetic pelitic system, uncertainty varies across P - T space with lower-temperature biotite- and garnet-zone conditions showing approximately double the uncertainty ($1\sigma = 25$ – 30 °C, 1.2 – 1.8 kbar) compared to higher-temperature sillimanite-zone conditions ($1\sigma = 16$ °C, 0.8 kbar). Across facies series, temperature uncertainty is highest in the low-pressure cordierite series ($1\sigma = 29$ °C) and lowest in the high-pressure kyanite series ($1\sigma = 16$ °C), whilst pressure uncertainty remains consistent ($1\sigma = 0.9$ – 1.1 kbar). The higher uncertainty at lower grades is mainly due to the impact of bulk composition uncertainty affecting inversions using modal volumes. Assemblage changes produces marked differences in uncertainty.

4. The source of uncertainty propagated and choice of input variables significantly impacts P - T estimates. Mineral composition variables generally yield lower uncertainties than modal volume variables. Accounting for mineral measurement uncertainty (bootstrapped at an appropriate percentage, $\sigma = \text{mean} \times \sim 20\%$) can capture the total quantifiable uncertainty stemming from the observations when using mineral composition variables. However, when modal volume variables are included, bulk composition uncertainty must also be accounted for, as it strongly influences phase stability boundaries. Where applicable, combining both variable types and propagating both mineral measurement and bulk composition uncertainties (observational uncertainty) may provide a more complete estimate of uncertainty in the system.

5. Given the varying sensitivities of different variables to uncertainty, selecting only those that minimize uncertainty may be misleading. Instead, the inversion should incorporate the largest and most diverse set of robust variables possible to ensure P - T estimates are representative of the natural system. This approach also enables an assessment of the overall model performance, which may provide insights into other characteristics of the system such as the degree of equilibrium.

SOFTWARE AVAILABILITY

1127 The outlined workflow, LinaForma, is available via the GitHub repository
1128 <https://github.com/TMackay-Champion/LinaForma>.

ACKNOWLEDGEMENTS

1129 T. Mackay-Champion would like to thank BHP and an Oxford-Radcliffe Graduate Scholar-
1130 ship for supporting his PhD research, and I.P. Cawood would like to acknowledge support from
1131 the Natural Environment Research Council (NERC; grant NE/L002612/1) and Hong Kong
1132 RGC Co-funding Mechanism on Joint Laboratories with the Chinese Academy of Science (grant
1133 JLFS/P-702/24 and 17308023). We thank journal reviewers Eleanor Greene and Geoff Clarke;
1134 and handling editor Katie Evans for suggestions that greatly improved the workflow, as well as
1135 the the clarity and content of the manuscript. We extend particular thanks to Dave Waters and
1136 Pierre Lanari for informal comments on the manuscript, Richard Palin for guidance over the
1137 course of this work, and Jacob Forshaw for fruitful discussions.

REFERENCES

- 1138 Belsley, D. A., E. Kuh, & R. E. Welsch (1980), Regression Diagnostics: Identifying Influential
1139 Data and Sources of Collinearity, Wiley, New York.
- 1140 Berman, R. G. (1991), Thermobarometry using multi-equilibrium calculations; a new technique,
1141 with petrological applications, *The Canadian Mineralogist*, 29, 833–855.
- 1142 Berman, R. G. (2007), winTWQ (version 2.3): A software package for performing internally-
1143 consistent thermobarometric calculations, Geological Survey of Canada, Open File, 5462.
- 1144 Bhatia, M. R. (1985), Rare earth element geochemistry of Australian Paleozoic graywackes
1145 and mudrocks: Provenance and tectonic control, *Sedimentary Geology*, 45(1), 97–113, doi:
1146 10.1016/0037-0738(85)90025-9.
- 1147 Blannin, R., M. Frenzel, L. Tuşa, S. Birtel, P. Ivăşcanu, T. Baker, & J. Gutzmer (2021), Uncer-
1148 tainties in quantitative mineralogical studies using scanning electron microscope-based image
1149 analysis, *Minerals Engineering*, 167, 106,836, doi:10.1016/j.mineng.2021.106836.
- 1150 Bucher, K., & M. Frey (1994), Metamorphism of Pelitic Rocks (Metapelites), in Petrogene-
1151 sis of Metamorphic Rocks, edited by K. Bucher & M. Frey, pp. 191–232, Springer, Berlin,
1152 Heidelberg, doi:10.1007/978-3-662-03000-4_7.
- 1153 Caddick, M. J., & A. B. Thompson (2008), Quantifying the tectono-metamorphic evolution of
1154 pelitic rocks from a wide range of tectonic settings: Mineral compositions in equilibrium,
1155 *Contributions to Mineralogy and Petrology*, 156(2), 177–195, doi:10.1007/s00410-008-0280-6.
- 1156 Carlson, W. D., D. R. Pattison, & M. J. Caddick (2015), Beyond the equilibrium paradigm:
1157 How consideration of kinetics enhances metamorphic interpretation, *American Mineralogist*,
1158 100(8-9), 1659–1667, doi:10.2138/am-2015-5097.
- 1159 Carmichael, D. M. (1978), Metamorphic bathozones and bathograds; a measure of the depth
1160 of post-metamorphic uplift and erosion on the regional scale, *American Journal of Science*,
1161 278(6), 769–797, doi:10.2475/ajs.278.6.769.
- 1162 Cawood, I. P., M. R. St-Onge, O. M. Weller, M. P. Searle, D. J. Waters, & T. Ahmad (2024),
1163 Structural and metamorphic architecture of the Zaskar Himalaya, Suru Valley region, NW
1164 India: Implications for the evolution of the Greater Himalayan Sequence, *GSA Bulletin*, doi:
1165 10.1130/B37241.1.

- 1166 Claerbout, J. F., & F. Muir (1973), Robust Modeling With Erratic Data, *Geophysics*, 38(5),
1167 826–844, doi:10.1190/1.1440378.
- 1168 Connolly, J. (1990), Multivariable phase diagrams: An algorithm based on generalized thermo-
1169 dynamics, *American Journal of Science*, 290, 666–718, doi:10.2475/ajs.290.6.666.
- 1170 Connolly, J. (2005), Computation of phase equilibria by linear programming: A tool for geody-
1171 namic modeling and its application to subduction zone decarbonation, *Earth and Planetary*
1172 *Science Letters*, 236(1-2), 524–541, doi:10.1016/j.epsl.2005.04.033.
- 1173 Copley, A., & O. Weller (2022), The controls on the thermal evolution of continental mountain
1174 ranges, *Journal of Metamorphic Geology*, 40(7), 1235–1270, doi:10.1111/jmg.12664.
- 1175 de Capitani, C., & T. H. Brown (1987), The computation of chemical equilibrium in complex
1176 systems containing non-ideal solutions, *Geochimica et Cosmochimica Acta*, 51(10), 2639–2652,
1177 doi:10.1016/0016-7037(87)90145-1.
- 1178 de Capitani, C., & K. Petrakakis (2010), The computation of equilibrium assemblage diagrams
1179 with Theriak/Domino software, *American Mineralogist*, 95(7), 1006–1016, doi:10.2138/am.
1180 2010.3354.
- 1181 Diener, J. F. A., & R. Powell (2010), Influence of ferric iron on the stability of mineral assem-
1182 blages, *Journal of Metamorphic Geology*, 28(6), 599–613, doi:10.1111/j.1525-1314.2010.00880.
1183 x.
- 1184 Doukkari, S. A., J. F. Diener, K. Ouzegane, & J.-R. Kienast (2018), Mineral equilibrium
1185 modelling and calculated chemical potential relations of reaction textures in the ultrahigh-
1186 temperature In Ouzzal terrane (In Hihaou area, Western Hoggar, Algeria), *Journal of Meta-*
1187 *morphic Geology*, 36(9), 1175–1198, doi:10.1111/jmg.12441.
- 1188 Droop, G. T. R. (1987), A general equation for estimating Fe³⁺ concentrations in ferromagnesian
1189 silicates and oxides from microprobe analyses, using stoichiometric criteria, *Mineralogical*
1190 *Magazine*, 51(361), 431–435, doi:10.1180/minmag.1987.051.361.10.
- 1191 Dubacq, B., & J. B. Forshaw (2024), The composition of metapelitic biotite, white mica, and
1192 chlorite: A review with implications for solid-solution models, *European Journal of Mineralogy*,
1193 36(4), 657–685, doi:10.5194/ejm-36-657-2024.
- 1194 Duesterhoeft, E., & P. Lanari (2020), Iterative thermodynamic modelling—Part 1: A theoret-

1195 ical scoring technique and a computer program (Bingo-Antidote), *Journal of Metamorphic*
1196 *Geology*, 38(5), 527–551, doi:10.1111/jmg.12538.

1197 Efron, B. (1979), Bootstrap Methods: Another Look at the Jackknife, *The Annals of Statistics*,
1198 7(1), 1–26, doi:10.1007/978-1-4612-4380-9_41.

1199 Evans, C. L., & T. J. Napier-Munn (2013), Estimating error in measurements of mineral grain
1200 size distribution, *Minerals Engineering*, 52, 198–203, doi:10.1016/j.mineng.2013.09.005.

1201 Forshaw, J. B., & D. R. Pattison (2023), Major-element geochemistry of pelites, *Geology*, 51(1),
1202 39–43, doi:10.1130/G50542.1.

1203 Forshaw, J. B., D. J. Waters, D. R. M. Pattison, R. M. Palin, & P. Gopon (2019), A comparison
1204 of observed and thermodynamically predicted phase equilibria and mineral compositions in
1205 mafic granulites, *Journal of Metamorphic Geology*, 37(2), 153–179, doi:10.1111/jmg.12454.

1206 Gervais, F., & P.-H. Trapy (2021), Testing solution models for phase equilibrium (forward)
1207 modeling of partial melting experiments, *Contributions to Mineralogy and Petrology*, 176(1),
1208 4, doi:10.1007/s00410-020-01762-5.

1209 Gordon, T. M. (1992), Generalized thermobarometry: Solution of the inverse chemical equi-
1210 librium problem using data for individual species, *Geochimica et Cosmochimica Acta*, 56(5),
1211 1793–1800, doi:10.1016/0016-7037(92)90310-F.

1212 Green, E. C. R., R. W. White, J. F. A. Diener, R. Powell, T. J. B. Holland, & R. M. Palin (2016),
1213 Activity–composition relations for the calculation of partial melting equilibria in metabasic
1214 rocks, *Journal of Metamorphic Geology*, 34(9), 845–869, doi:10.1111/jmg.12211.

1215 Guevara, V. E., & M. J. Caddick (2016), Shooting at a moving target: Phase equilibria modelling
1216 of high-temperature metamorphism, *Journal of Metamorphic Geology*, 34(3), 209–235, doi:
1217 10.1111/jmg.12179.

1218 Guiraud, M., R. Powell, & G. Rebay (2001), H₂O in metamorphism and unexpected behaviour
1219 in the preservation of metamorphic mineral assemblages, *Journal of Metamorphic Geology*,
1220 19(4), 445–454, doi:10.1046/j.0263-4929.2001.00320.x.

1221 Hawthorne, F., R. Oberti, G. Harlow, W. Maresch, R. Martin, J. Schumacher, & M. Welch
1222 (2012), Nomenclature of the amphibole supergroup, *American Mineralogist*, 97, 2031–2048.

1223 Henry, D. J., & C. V. Guidotti (2002), Titanium in biotite from metapelitic rocks: Temperature

- 1224 effects, crystal-chemical controls, and petrologic applications, *American Mineralogist*, 87(4),
1225 375–382, doi:10.2138/am-2002-0401.
- 1226 Henry, D. J., C. V. Guidotti, & J. A. Thomson (2005), The Ti-saturation surface for low-to-
1227 medium pressure metapelitic biotites : Implications for geothermometry and Ti-substitution
1228 mechanisms, *American Mineralogist*, 90, 316–328, doi:10.2138/am.2005.1498.
- 1229 Hodges, K. V., & P. D. Crowley (1985), Error estimation and empirical geothermobarometry
1230 for pelitic systems., *American Mineralogist*, 70(7-8), 702–709.
- 1231 Hodges, K. V., & L. W. McKenna (1987), Realistic propagation of uncertainties in geologic
1232 thermobarometry, *American Mineralogist*, 72(7-8), 671–680.
- 1233 Hofer, H. E., G. P. Brey, B. Schulz-Dobrick, & R. Oberhänsli (1994), The determination of
1234 the oxidation state of iron by the electron microprobe, *European Journal of Mineralogy*, pp.
1235 407–418, doi:10.1127/ejm/6/3/0407.
- 1236 Holland, T., & J. Blundy (1994), Non-ideal interactions in calcic amphiboles and their bearing
1237 on amphibole-plagioclase thermometry, *Contributions to Mineralogy and Petrology*, 116(4),
1238 433–447, doi:10.1007/BF00310910.
- 1239 Holland, T., & R. Powell (1996a), Thermodynamics of order-disorder in minerals; I, Symmetric
1240 formalism applied to minerals of fixed composition, *American Mineralogist*, 81(11-12), 1413–
1241 1424, doi:10.2138/am-1996-11-1214.
- 1242 Holland, T., & R. Powell (1996b), Thermodynamics of order-disorder in minerals: II. Symmetric
1243 formalism applied to solid solutions, *American Mineralogist*, 81(11-12), 1425–1437, doi:10.
1244 2138/am-1996-11-1215.
- 1245 Holland, T., & R. Powell (2003), Activity–composition relations for phases in petrological calcu-
1246 lations: An asymmetric multicomponent formulation, *Contributions to Mineralogy and Petrol-*
1247 *ogy*, 145(4), 492–501, doi:10.1007/s00410-003-0464-z.
- 1248 Holland, T. J. B., & R. Powell (1998), An internally consistent thermodynamic data set for
1249 phases of petrological interest, *Journal of Metamorphic Geology*, 16(3), 309–343, doi:10.1111/
1250 j.1525-1314.1998.00140.x.
- 1251 Holland, T. J. B., & R. Powell (2011), An improved and extended internally consistent thermo-

dynamic dataset for phases of petrological interest, involving a new equation of state for solids,
Journal of Metamorphic Geology, 29(3), 333–383, doi:10.1111/j.1525-1314.2010.00923.x.

Hollister, L. (1969), Contact Metamorphism in the Kwoiek Area of British Columbia: An
 End Member of the Metamorphic Process, *GSA Bulletin*, 80(12), 2465–2494, doi:10.1130/
 0016-7606(1969)80[2465:CMITKA]2.0.CO;2.

Hoschek, G. (2004), Comparison of calculated P-T pseudosections for a kyanite eclogite from
 the Tauern Window, Eastern Alps, Austria, *European Journal of Mineralogy*, pp. 59–72, doi:
 10.1127/0935-1221/2004/0016-0059.

Ibraheem, I. M., B. Tezkan, & R. Bergers (2021), Integrated Interpretation of Magnetic and ERT
 Data to Characterize a Landfill in the North-West of Cologne, Germany, *Pure and Applied
 Geophysics*, 178(6), 2127–2148, doi:10.1007/s00024-021-02750-x.

Kendrick, J., & A. Indares (2018), The reaction history of kyanite in high-P aluminous granulites,
Journal of Metamorphic Geology, 36(2), 125–146, doi:10.1111/jmg.12286.

Kohn, M. J., & F. S. Spear (1991a), Error propagation for barometers: 1. Accuracy and precision
 of experimentally located end member reactions, *American Mineralogist*, 76, 128–137.

Kohn, M. J., & F. S. Spear (1991b), Error propagation for barometers: 2. Application to rocks,
American Mineralogist, 76, 138–147.

Lanari, P., & E. Duisterhoeft (2019), Modeling Metamorphic Rocks Using Equilibrium Thermo-
 dynamics and Internally Consistent Databases: Past Achievements, Problems and Perspec-
 tives, *Journal of Petrology*, 60(1), 19–56, doi:10.1093/petrology/egy105.

Lanari, P., & M. Engi (2017), Local Bulk Composition Effects on Metamorphic Min-
 eral Assemblages, *Reviews in Mineralogy and Geochemistry*, 83(1), 55–102, doi:10.1016/
 B978-0-08-102908-4.00135-1.

Lanari, P., & J. Hermann (2021), Iterative thermodynamic modelling—Part 2: Tracing equilib-
 rium relationships between minerals in metamorphic rocks, *Journal of Metamorphic Geology*,
 39(6), 651–674, doi:10.1111/jmg.12575.

Lanari, P., S. Ferrero, P. Goncalves, & E. G. Grosch (2019), Metamorphic geology: Progress
 and perspectives, *Geological Society, London, Special Publications*, 478(1), 1–12, doi:10.1144/
 SP478-2018-186.

- 1281 Li, C.-N., Y.-H. Shao, & N.-Y. Deng (2015), Robust L1-norm two-dimensional linear discrimi-
1282 nant analysis, *Neural Networks*, 65, 92–104, doi:10.1016/j.neunet.2015.01.003.
- 1283 McLennan, S. M., S. Hemming, D. K. McDaniel, & G. N. Hanson (1993), Geochemical ap-
1284 proaches to sedimentation, provenance, and tectonics, *Processes Controlling the Composition*
1285 *of Clastic Sediments*, p. 0, doi:10.1130/SPE284-p21.
- 1286 Menke, W. (1984), Geophysical Data Analysis: Discrete Inverse Theory, Academic Press, Or-
1287 lando.
- 1288 Ohmoto, H., & D. M. Kerrick (1977), Devolatilization equilibria in graphitic systems, *American*
1289 *Journal of Science*, 277(8), 1013–1044, doi:10.2475/ajs.277.8.1013.
- 1290 Palin, R. M., O. M. Weller, D. J. Waters, & B. Dyck (2016), Quantifying geological uncertainty
1291 in metamorphic phase equilibria modelling; a Monte Carlo assessment and implications for
1292 tectonic interpretations, *Geoscience Frontiers*, 7(4), 591–607, doi:10.1016/j.gsf.2015.08.005.
- 1293 Pattison, D. R. M., & C. L. DeBuhr (2015), Petrology of metapelites in the Bugaboo aureole,
1294 British Columbia, Canada, *Journal of Metamorphic Geology*, 33(5), 437–462, doi:10.1111/
1295 jmg.12128.
- 1296 Pattison, D. R. M., & S. A. Goldsmith (2022), Metamorphism of the Buchan type-area, NE
1297 Scotland and its relation to the adjacent Barrovian domain, *Journal of the Geological Society*,
1298 179, jgs2021–040.
- 1299 Pattison, D. R. M., & F. S. Spear (2018), Kinetic control of staurolite–Al₂SiO₅ mineral as-
1300 semblages: Implications for Barrovian and Buchan metamorphism, *Journal of Metamorphic*
1301 *Geology*, 36(6), 667–690, doi:10.1111/jmg.12302.
- 1302 Pattison, D. R. M., & D. K. Tinkham (2009), Interplay between equilibrium and kinetics in
1303 prograde metamorphism of pelites: An example from the Nelson aureole, British Columbia,
1304 *Journal of Metamorphic Geology*, 27(4), 249–279, doi:10.1111/j.1525-1314.2009.00816.x.
- 1305 Pattison, D. R. M., & R. J. Tracy (1991), Phase equilibria and thermobarometry of metapelites,
1306 *Reviews in Mineralogy & Geochemistry*, 26, 106–206.
- 1307 Powell, R. (1985), Geothermometry and geobarometry: A discussion, *Journal of the Geological*
1308 *Society*, 142(1), 29–38, doi:10.1144/gsjgs.142.1.0029.
- 1309 Powell, R., & T. Holland (1988), An internally consistent dataset with uncertainties and corre-

1310 lations: 3. Applications to geobarometry, worked examples and a computer program, *Journal*
 1311 *of Metamorphic Geology*, 6(2), 173–204, doi:10.1111/j.1525-1314.1988.tb00415.x.

1312 Powell, R., & T. Holland (1993a), The applicability of least squares in the extraction of ther-
 1313 modynamic data from experimentally bracketed mineral equilibria, *American Mineralogist*,
 1314 78(1-2), 107–112.

1315 Powell, R., & T. Holland (1993b), On the formulation of simple mixing models for complex
 1316 phases, *American Mineralogist*, 78(11-12), 1174–1180.

1317 Powell, R., & T. Holland (1994), Optimal geothermometry and geobarometry, *American Min-*
 1318 *eralogist*, 79, 120–133.

1319 Powell, R., & T. J. B. Holland (2008), On thermobarometry, *Journal of Metamorphic Geology*,
 1320 26(2), 155–179, doi:10.1111/j.1525-1314.2007.00756.x.

1321 Riel, N., B. J. P. Kaus, E. C. R. Green, & N. Berlie (2022), MAGEMin, an Efficient Gibbs
 1322 Energy Minimizer: Application to Igneous Systems, *Geochemistry, Geophysics, Geosystems*,
 1323 23(7), e2022GC010,427, doi:10.1029/2022GC010427.

1324 Roser, B. P., & R. J. Korsch (1988), Provenance signatures of sandstone-mudstone suites deter-
 1325 mined using discriminant function analysis of major-element data, *Chemical Geology*, 67(1),
 1326 119–139, doi:10.1016/0009-2541(88)90010-1.

1327 Schorn, S., & J. F. Diener (2019), Seemingly disparate temperatures recorded in coexisting
 1328 granulite facies lithologies, *Journal of Metamorphic Geology*, 37(8), 1049–1078, doi:10.1111/
 1329 jmg.12500.

1330 Schumacher, J. C. (1991), Empirical ferric iron corrections: Necessity, assumptions, and ef-
 1331 fects on selected geothermobarometers, *Mineralogical Magazine*, 55(378), 3–18, doi:10.1180/
 1332 minmag.1991.055.378.02.

1333 Spear, F. S., D. R. Pattison, & J. T. Cheney (2016), The metamorphism of metamorphic petrol-
 1334 ogy, in *The Web of Geological Sciences: Advances, Impacts, and Interactions II: Geological*
 1335 *Society of America Special Paper 523*, edited by M. Bickford, The Geological Society of Amer-
 1336 ica, doi:10.1130/2016.2523(02).

1337 Starr, P. G., & D. R. M. Pattison (2019), Equilibrium and disequilibrium processes across

- 1338 the greenschist–amphibolite transition zone in metabasites, *Contributions to Mineralogy and*
 1339 *Petrology*, 174(2), 18, doi:10.1007/s00410-019-1553-y.
- 1340 Starr, P. G., D. R. M. Pattison, & D. E. Ames (2020), Mineral assemblages and phase equilibria
 1341 of metabasites from the prehnite–pumpellyite to amphibolite facies, with the Flin Flon Green-
 1342 stone Belt (Manitoba) as a type example, *Journal of Metamorphic Geology*, 38(1), 71–102,
 1343 doi:10.1111/jmg.12513.
- 1344 Steltenpohl, M. G., & J. M. Bartley (1987), Thermobarometric profile through the Caledonian
 1345 nappe stack of Western Ofoten, North Norway, *Contributions to Mineralogy and Petrology*,
 1346 96(1), 93–103, doi:10.1007/BF00375530.
- 1347 Štípská, P., & R. Powell (2005), Constraining the P–T path of a MORB-type eclogite using
 1348 pseudosections, garnet zoning and garnet-clinopyroxene thermometry: An example from the
 1349 Bohemian Massif, *Journal of Metamorphic Geology*, 23(8), 725–743, doi:10.1111/j.1525-1314.
 1350 2005.00607.x.
- 1351 Stüwe, K. (1997), Effective bulk composition changes due to cooling: A model predicting com-
 1352 plexities in retrograde reaction textures, *Contributions to Mineralogy and Petrology*, 129(1),
 1353 43–52, doi:10.1007/s004100050322.
- 1354 Stüwe, K., & R. Powell (1995), PT Paths from modal proportions: Application to the Ko-
 1355 ralm Complex, Eastern Alps | Contributions to Mineralogy and Petrology, *Contributions to*
 1356 *Mineralogy and Petrology*, 119, 83–93.
- 1357 Thompson, A. B. (1986), The Role of Mineral Kinetics in the Development of Metamorphic
 1358 Microtextures, in Fluid–Rock Interactions during Metamorphism, vol. 5, edited by S. K.
 1359 Saxena, J. V. Walther, & B. J. Wood, pp. 154–193, Springer New York, New York, NY,
 1360 doi:10.1007/978-1-4612-4896-5_7.
- 1361 Tinkham, D. K., C. A. Zuluaga, & H. H. Stowell (2001), Metapelite phase equilibria modeling in
 1362 MnNCKFMASH: The effect of variable Al₂O₃ and MgO/(MgO + FeO) on mineral stability,
 1363 *Geological Materials Research*, 3(1), 1–42.
- 1364 Van der Plas, L., & A. C. Tobi (1965), A chart for judging the reliability of point counting
 1365 results, *American Journal of Science*, 263(1), 87–90, doi:10.2475/ajs.263.1.87.
- 1366 Vance, D., & E. Mahar (1998), Pressure-temperature paths from P–T pseudosections and zoned

garnets: Potential, limitations and examples from the Zaskar Himalaya, NW India, *Contributions to Mineralogy and Petrology*, 132, 225–245.

Verma, S. P., & J. S. Armstrong-Altrin (2016), Geochemical discrimination of siliciclastic sediments from active and passive margin settings, *Sedimentary Geology*, 332, 1–12, doi: 10.1016/j.sedgeo.2015.11.011.

Voll, G., J. Töpel, D. R. M. Pattison, & F. Seifert (Eds.) (1991), Equilibrium and Kinetics in Contact Metamorphism, Springer, Berlin, Heidelberg, doi:10.1007/978-3-642-76145-4.

Waters, D. J. (2019), Metamorphic constraints on the tectonic evolution of the High Himalaya in Nepal: The art of the possible, *Geological Society London, Special Publication*, 483, doi: 10.1144/sp483-2018-187.

Waters, D. J., & D. P. Lovegrove (2002), Assessing the extent of disequilibrium and overstepping of prograde metamorphic reactions in metapelites from the Bushveld Complex aureole, South Africa, *Journal of Metamorphic Geology*, 20(1), 135–149, doi:10.1046/j.0263-4929.2001.00350.x.

Weller, O. M., M. R. St-Onge, D. J. Waters, N. Rayner, M. P. Searle, S.-L. Chung, R. M. Palin, Y.-H. Lee, & X. Xu (2013), Quantifying Barrovian metamorphism in the Danba Structural Culmination of eastern Tibet, *Journal of Metamorphic Geology*, 31(9), 909–935, doi:10.1111/jmg.12050.

Weller, O. M., T. J. B. Holland, C. R. Soderman, E. C. R. Green, R. Powell, C. D. Beard, & N. Riel (2024), New Thermodynamic Models for Anhydrous Alkaline-Silicate Magmatic Systems, *Journal of Petrology*, 65(10), egae098, doi:10.1093/petrology/egae098.

Wheeler, J., L. S. Mangan, & D. J. Prior (2004), Disequilibrium in the Ross of Mull Contact Metamorphic Aureole, Scotland: A Consequence of Polymetamorphism, *Journal of Petrology*, 45(4), 835–853, doi:10.1093/petrology/egg113.

White, R. W., R. Powell, & T. J. B. Holland (2007), Progress relating to calculation of partial melting equilibria for metapelites, *Journal of Metamorphic Geology*, 25(5), 511–527, doi:10.1111/j.1525-1314.2007.00711.x.

Worley, & Powell (2000), High-precision relative thermobarometry: Theory and a worked example, *Journal of Metamorphic Geology*, 18(1), 91–101, doi:10.1046/j.1525-1314.2000.00239.x.

1396 Yardley, B. W. D. (1977), The nature and significance of the mechanism of sillimanite growth
1397 in the Connemara schists, Ireland, *Contributions to Mineralogy and Petrology*, 65(1), 53–58,
1398 doi:10.1007/BF00373570.

FIGURE CAPTIONS

1399 Figure 1: Schematic summary of the primary sources of uncertainty in thermobarometry, de-
1400 tailing their propagation (where quantifiable) into P - T solution uncertainties. Observational
1401 uncertainties can be calculated using the new workflow presented in this study, LinaForma, or
1402 predictive uncertainties (specifically those stemming from model uncertainty) can be calculated
1403 using avPT mode in THERMOCALC (Powell & Holland, 1994).

1404 Figure 2: Schematic summary of (a–d) common problems associated with application of inter-
1405 secting mineral composition variables commonly applied in constraining the P - T conditions from
1406 forward models. (e) Using a large and diverse range of robust mineral composition variables to
1407 provide a more representative P - T constraint. Definitions of mineral composition variables are
1408 included in Table 1 for reference.

1409 Figure 3: Schematic summary of the presented workflow and methods. From observations and
1410 forward modelling of a given rock system to (a) grid-search non-linear inversion to determine
1411 the best-fit P - T conditions, to (b) bootstrap-resampling to assess the uncertainty of the P - T
1412 solution, and (c) result diagnostic using bootstrap resampling of the employed variables to assess
1413 sensitivity of the best-fit result to uncertainty in the individual variables. Thin-section schematic
1414 from Palin *et al.* (2016).

1415 Figure 4: Workflow example using natural sample ICSV13. (a) Overlapping isopleth “fields”
1416 defined by 2σ range of mineral measurements. (b) Intersection of X_{Gr} , X_{Prp} , and X_{SpS} isopleth
1417 fields defined by 2σ range of mineral measurements. (c) Grid-search best-fit solutions and
1418 heatmap (error-surface) for bootstrapped mineral measurement data ($n = 1000$), overlain with
1419 the bootstrapped mean and median best-fit result. (d) Data residuals at the median P - T point
1420 of 576°C and 9.53 kbar , showing the fit between the model and the observations. (e) Sensitivity
1421 analysis for T and P of mineral composition variables presented as tornado plots at the mean
1422 P - T point of 577°C and 9.64 kbar .

Figure 5: Example of compiled final result of ICSV13 (a–e) and ICSV117 (f–j). (a, f) Pseudo-section. (b, g) Heatmap (error-surface) of best-fit solutions showing the misfit of mineral composition variables, overlain with the corresponding pseudosection and the bootstrapped mean best-fit result and 1σ uncertainty. (c, h) Boxplots of bootstrapped T and P estimates with the grey bar indicating the range of the selected thermometer and avP results. (d, i) Log-scaled 2D-histogram bin-plot of the bootstrapped data with mean best-fit result marked by the star. (e, j) % overlap of peak compositional isopleth fields.

Figure 6: Uncertainty (1σ) in P - T estimate as a result of mineral measurement uncertainty (MMU). (a) Uncertainty in T using composition variables. (b) Uncertainty in P using composition variables. (c) Uncertainty in T using modal volume variables. (d) Uncertainty in P using modal volume variables. (e) Uncertainty in T using both composition and modal volume variables. (f) Uncertainty in P using both composition and modal volume variables. (g) The distribution of T uncertainty over modeled P - T space. (h) The distribution of P uncertainty over modeled P - T space. Composition relates to composition variables only. Volume relates to modal volume variables only. Combined relates to composition and modal volume variables together. Bt = biotite, Grt = garnet, and Porph = porphyroblast (cordierite/andalusite/staurolite/kyanite).

Figure 7: A) Uncertainty (1σ) in P - T estimate as a result of bulk composition uncertainty (BCU). (a) Uncertainty in T using composition variables. (b) Uncertainty in P using composition variables. (c) Uncertainty in T using modal volume variables. (d) Uncertainty in P using modal volume variables. (e) Uncertainty in T using both composition and modal volume variables. (f) Uncertainty in P using both composition and modal volume variables. (g) The distribution of T uncertainty over modeled P - T space. (h) The distribution of P uncertainty over modeled P - T space. Composition = composition variables only. Volume = modal volume variables only. Combined = composition and modal volume variables together. Bt = biotite, Grt = garnet, and Porph = porphyroblast (cordierite/andalusite/staurolite/kyanite).

Figure 8: Uncertainty (1σ) in P - T estimate as a result of observational uncertainty (OU , mineral measurement uncertainty and bulk composition uncertainty combined). (a) Uncertainty in T using composition variables. (b) Uncertainty in P using composition variables. (c) Uncertainty in T using modal volume variables. (d) Uncertainty in P using modal volume variables. (e) Uncertainty in T using both composition and modal volume variables. (f) Uncertainty in P using both composition and modal volume variables. (g) The distribution of T uncertainty over modeled P - T space. Composition relates to composition variables only. Volume relates to modal volume variables only. (h) The distribution of P uncertainty over modeled P - T space. Composition = composition variables only. Volume = modal volume variables only. Combined = composition and modal volume variables together. Bt = biotite, Grt = garnet, and Porph = porphyroblast (cordierite/andalusite/stauroilite/kyanite).

Figure 9: The distribution of uncertainty in T and P binned into different metamorphic zones and facies series. (a) T uncertainty only using composition variables. (b) P uncertainty only using composition variables. (c) T uncertainty only using modal volume variables. (d) P uncertainty only using modal volume variables. (e) T uncertainty using both composition and modal volume variables. (f) P uncertainty using both composition and modal volume variables.

Figure 10: The uncertainty in T and P for each variable as a result of mineral measurement uncertainty (MMU), bulk composition uncertainty (BCU), and observational uncertainty (OU , MMU and BCU combined). (a) T uncertainty for composition variables. (b) P uncertainty for composition variables. (c) T uncertainty for modal volume variables. (d) P uncertainty for modal volume variables.

Figure 11: The change of uncertainty in T and P along a geotherm as a result of mineral measurement uncertainty (MMU) at 10 % of the mean, MMU at 20 % of the mean, bulk composition uncertainty (BCU), and observational uncertainty (OU , a combination of MMU at 10 % of the mean and BCU). (a) Uncertainty in T using composition variables. (b) Uncertainty in T using modal volume variables. (c) Uncertainty in T using both composition and modal volume variables. (d) Uncertainty in P using composition variables. (e) Uncertainty in P using modal volume variables. (f) Uncertainty in P using both composition and modal volume variables. (g, h) Modal abundance of phases along the geotherm.

Table 1: Mineral composition variable definitions for common pelitic and metabasic minerals at sub-solidus conditions.

Mineral	Variable	Definition
Grt	X_{Alm}	$\frac{\text{Fe}^{2+}}{\text{Fe}^{2+} + \text{Mg} + \text{Ca} + \text{Mn}}$
	X_{Grs}	$\frac{\text{Ca}}{\text{Fe}^{2+} + \text{Mg} + \text{Ca} + \text{Mn}}$
	X_{Sps}	$\frac{\text{Mn}}{\text{Fe}^{2+} + \text{Mg} + \text{Ca} + \text{Mn}}$
	X_{Prp}	$\frac{\text{Mg}}{\text{Fe}^{2+} + \text{Mg} + \text{Ca} + \text{Mn}}$
	X_{Mg}	$\frac{\text{Mg}}{\text{Mg} + \text{Fe}^{2+}}$
Grt (without Mn)	X_{Alm}	$\frac{\text{Fe}^{2+}}{\text{Fe}^{2+} + \text{Mg} + \text{Ca}}$
	X_{Grs}	$\frac{\text{Ca}}{\text{Fe}^{2+} + \text{Mg} + \text{Ca}}$
	X_{Prp}	$\frac{\text{Mg}}{\text{Fe}^{2+} + \text{Mg} + \text{Ca}}$
	X_{Mg}	$\frac{\text{Mg}}{\text{Mg} + \text{Fe}^{2+}}$
St	X_{Mg}	$\frac{\text{Mg}}{\text{Mg} + \text{Fe}^{2+}}$
Crd	X_{Mg}	$\frac{\text{Mg}}{\text{Mg} + \text{Fe}^{2+}}$
Chl	X_{Mg}	$\frac{\text{Mg}}{\text{Mg} + \text{Fe}^{2+}}$
Bt	Si	apfu
	Ti	apfu
	X_{Mg}	$\frac{\text{Mg}}{\text{Mg} + \text{Fe}^{2+}}$
Ms	Si	apfu
	X_{Cel}	Mg apfu
	X_{Pa}	$\frac{\text{Na}}{\text{Na} + \text{Ca} + \text{K}}$
Pl	X_{Ab}	$\frac{\text{Na}}{\text{Na} + \text{Ca} + \text{K}}$
Kfs	X_{San}	$\frac{\text{K}}{\text{Na} + \text{Ca} + \text{K}}$
Ep	X_{Fe}	$\frac{\text{Fe}^{3+}}{\text{Al} + \text{Fe}^{3+}}$
Amph	Ts vector	$\text{Al}(\text{T}) - \text{Na}(\text{A}) - \text{K}(\text{A})$
	Ed vector	$\text{Na}(\text{A}) + \text{K}(\text{A})$
	Gln vector	$\text{Na}(\text{M4})$
	Ti	apfu
Cpx	Al	apfu
	X_{Mg}	$\frac{\text{Mg}}{\text{Mg} + \text{Fe}^{2+}}$
	Ca	apfu
	X_{Jd}	$\frac{\text{Al}^{VI}}{\text{Na} + \text{Ca}}$

Table 2: Definitions of parameters used in the inversion analysis and presented in the result output and diagnostics table.

Parameter	Definition
X_i	Quality of fit score for each variable. Higher values indicate a poorer fit.
ΔT	Maximum absolute temperature variation due to uncertainty in a variable, relative to the mean best-fit solution.
ΔP	Maximum absolute pressure variation due to uncertainty in a variable, relative to the mean best-fit solution.
$\mu_{\text{obs}} \pm 2\sigma$	Mean observed variable value, with two standard deviations (uncertainty).
Pred	Predicted value of variable for the median best-fit solution.
Mean	Average temperature and pressure of the solution distribution (1σ).
Median	50th percentile of the temperature and pressure distribution.
IQR	Interquartile range (25th–75th percentile) of the temperature and pressure distribution.
X_{total}	Overall quality of fit score for the inversion; values above 1 suggest poor fit.
SE	Standard error, expressed as a percentage relative to the mean solution.
# of fitted variables	Total number of data successfully fitted by the inversion (out of total).
Grid resolution	Precision/spacing of the grid in °C and kbar
Bootstrap resamples	Number of bootstrap resamples

Table 3: Measured bulk composition via XRF of ICSV13 and ICSV117 in wt%.

Sample	SiO₂	Al₂O₃	Fe₂O₃	MnO	MgO	CaO	Na₂O	K₂O	TiO₂	P₂O₅	LOI	Total
ICSV13	61.23	19.13	7.10	0.09	2.65	0.47	1.52	4.12	0.98	0.09	1.96	99.31
ICSV117	47.80	14.42	14.92	0.19	6.39	9.99	2.41	0.75	2.12	0.18	0.34	99.51

Table 4: Variables used for parametric bootstrap resampling in ICSV13 and ICSV117 (rounded to 3 decimal places).

Mineral	Garnet				Biotite			Muscovite			Plagioclase		Amphibole			
Variable	X_{Grs}	X_{Sps}	X_{Prp}	X_{Mg}	Si	Ti	X_{Mg}	Si	X_{Cel}	X_{Pa}	X_{Ab}	Ts	Ed	Gln	Ti	
ICSV13																
Mean	0.059	0.019	0.164	0.177	2.713	0.102	0.490	3.068	0.079	0.230	0.888					
SD	0.007	0.004	0.011	0.011	0.016	0.005	0.003	0.023	0.011	0.015	0.036					
ICSV117																
Mean					2.764	0.147	0.490				0.792	1.189	0.487	0.150	0.085	
SD					0.005	0.009	0.015				0.012	0.034	0.028	0.010	0.012	

Table 5: Result output and diagnostics for ICSV13.

Variable	X_i	ΔT (°C)	ΔP (kbar)	μ_{obs} + 2σ	μ_{obs} - 2σ	Pred
X_{Grs}	0.08957	7.418	0.3735	0.0724	0.0459	0.0580
X_{Sps}	0.1844	7.849	0.7638	0.0266	0.0108	0.0202
X_{Prp}	0.9927	3.697	0.323	0.1857	0.1415	0.1855
$X_{\text{Mg Grt}}$	0.9063	3.726	0.3268	0.1992	0.1556	0.1972
Si Bt	0.5486	0.8295	0.1951	2.744	2.682	2.730
Ti Bt	0.6898	3.44	0.3789	0.1111	0.0929	0.0958
Si Ms	0.304	0.8295	0.1951	3.115	3.021	3.054
X_{Pa}	0.142	9.43	0.2775	0.2597	0.2006	0.2343
X_{Ab}	0.1607	3.301	3.301	0.9596	0.8155	0.8991
Mean = 577 ± 6 °C, 9.64 ± 0.57 kbar (1σ)						
Median = 576 °C (IQR = 573–582 °C), 9.53 kbar (IQR = 9.28–9.85 kbar)						
X_{total} (median) = 0.446						
SE (mean) = 2 °C (0.347 %), 0.19 kbar (1.99 %)						
# of fitted variables = 9/9						
Model resolution = 3.03 °C, 0.0808 kbar						
Bootstrap resamples = 1000						

Table 6: Result output and diagnostics for ICSV117.

Variable	X_i	ΔT (°C)	ΔP (kbar)	μ_{obs} + 2σ	μ_{obs} - 2σ	Pred
Ti Bt	0.1017	29.22	0.4183	0.1650	0.1298	0.1492
X _{Mg} Bt	0.3689	9.136	0.1529	0.5210	0.4596	0.5016
X _{Ab}	1.481	1.689	0.001453	0.8162	0.7686	0.7572
Ts	1.727	1.689	0.001453	1.257	1.121	1.307
Gln	0.02863	6.099	0.4547	0.1697	0.1311	0.1499
Ti Amph	1.485	4.16	0.03779	0.1097	0.0597	0.0476
Mean = 669 ± 14 °C, 11.82 ± 0.29 kbar (1σ)						
Median = 669 °C (IQR = 659–677 °C), 11.82 kbar (IQR = 11.66–11.98 kbar)						
X _{total} (median) = 0.865						
SE (mean) = 6 °C (0.897 %), 0.12 kbar (1.02 %)						
# of fitted variables = 3/6						
Model resolution = 2.02 °C, 0.0808 kbar						
Bootstrap resamples = 1000						

Table 7: Standard deviation of each oxide mol% applied to the worldwide median pelite bulk composition used in the Monte-Carlo simulation.

Oxide	SiO₂	TiO₂	Al₂O₃	FeO	O	MnO	MgO	CaO	Na₂O	K₂O
Mean	57.00	0.61	10.29	4.58	0.25	0.06	3.19	0.62	1.19	2.24
SD	0.52	0.09	0.26	0.46	0.02	0.02	0.22	0.24	0.12	0.15

Table 8: Median temperature and pressure uncertainty across different metamorphic zones and facies series. "C" is composition variables. "V" is modal volume variables.

		Median T uncertainty (1σ , °C)			Median P uncertainty (1σ , kbar)		
		$C + V$	C	V	$C + V$	C	V
Metamorphic zone	Biotite zone	30	29	46	1.8	1.0	2.2
	Garnet zone	25	16	38	1.2	0.8	2.0
	Porphyroblast zone	16	14	28	0.8	0.7	1.2
	Sillimanite zone	16	17	29	0.8	0.8	0.9
Facies series	Cordierite series	29	24	49	0.9	0.7	1.3
	Staurolite series	23	20	37	1.1	0.8	1.7
	Kyanite series	16	12	27	1.0	0.7	1.3
P - T space	All zones and series	21	16	36	1.0	0.8	1.4

Figure 1

User choice

X

Geological

- ☒ Sampling bias and natural inhomogeneity
- ☒ Interpreted scale of equilibrium
- ☐ Disequilibrium processes
- ☐ Selection of equilibrium assemblage

Analytical

- Mineral compositions
- Mineral modes

Parameter

- Choice of thermodynamic database, a - X models, model system, P - T - X range and precision
- Input parameters ($X\text{Fe}^{3+}$, $a\text{H}_2\text{O}$, $M\text{H}_2\text{O}$)

Model

- ☐ Formulation of model
- ☒ Enthalpies of formation
- ☒ Activity coefficient & interaction parameters

Observational

-

Bulk composition
uncertainty

-

Mineral measurement uncertainty

Predictive

-

- Model setup uncertainty

-

Input parameter uncertainty

-

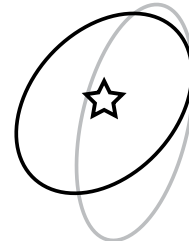
- Thermodynamic dataset uncertainty

-

End-member activity
uncertainty

P (kbar)

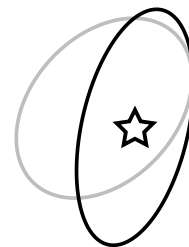
Observational



LingForma

 $T (^{\circ}\text{C})$ P (kbar)

Predictive

 $qvPT$ $T (^{\circ}\text{C})$

- Quantifiable ◐ Semi-quantifiable
 ○ Unquantifiable

**Dependent on method of bulk rock acquisition*

☆ peak result ○ 1 sd ellipse

'Fixed'

selectively chosen variables

all variables

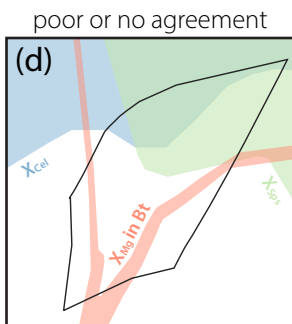
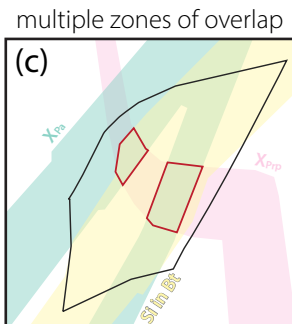
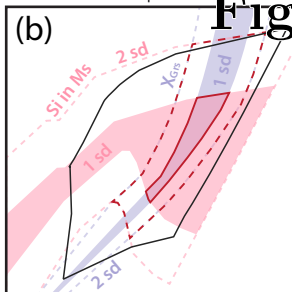
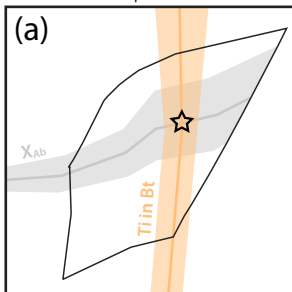
too precise

variable precision

peak point and associated uncertainty

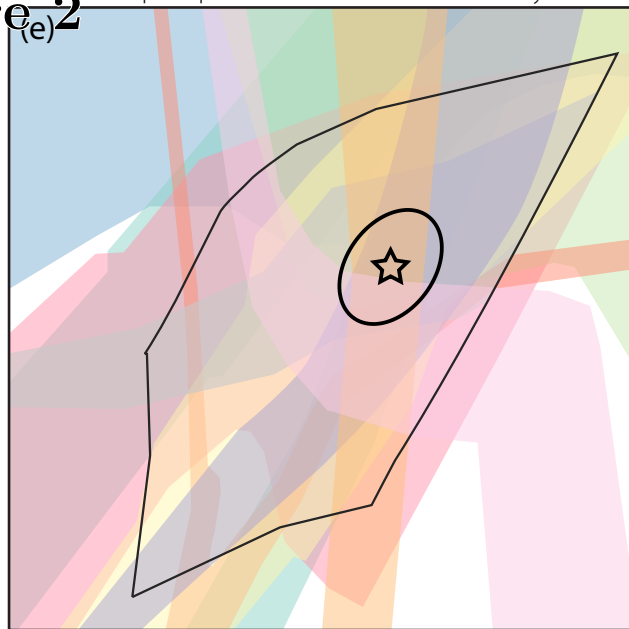
Figure 2

P (kbar)



T ($^{\circ}C$)

P (kbar)



T ($^{\circ}C$)

variables

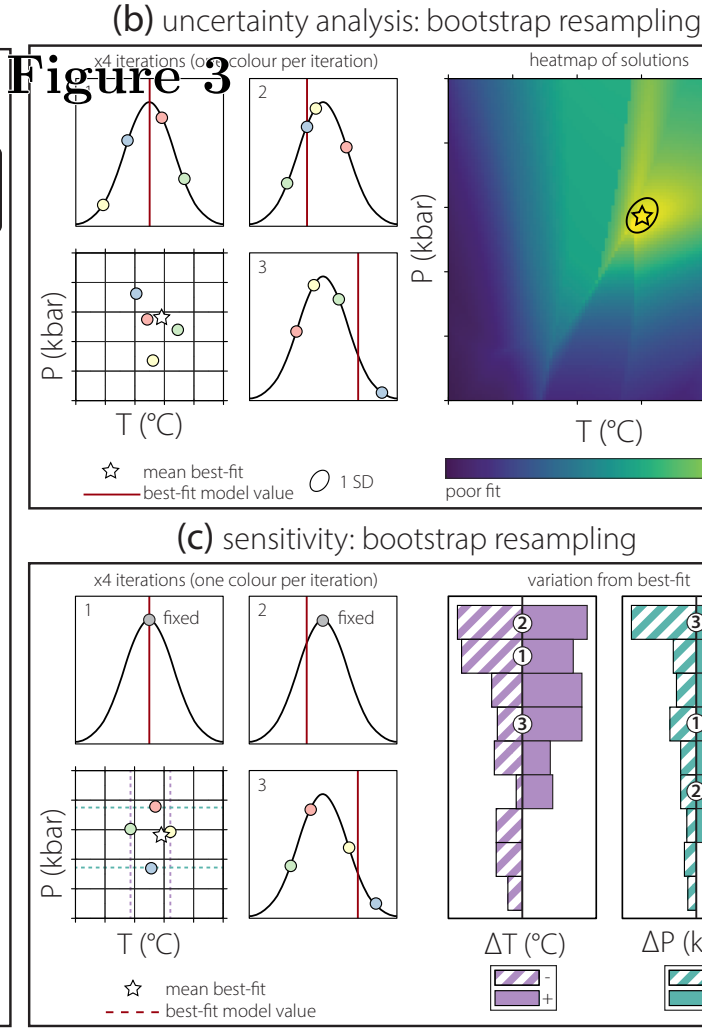
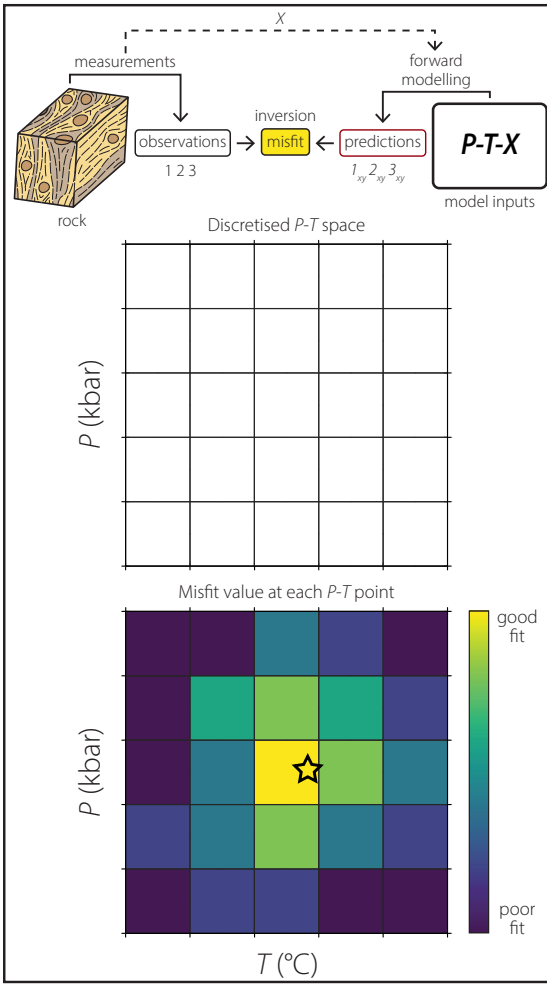
Grt	Bt	Ms
X_{Prp}	Si	Si
X_{Sp}	Ti	X_{Cel}
X_{Grs}	X_{Mg}	X_{Pa}

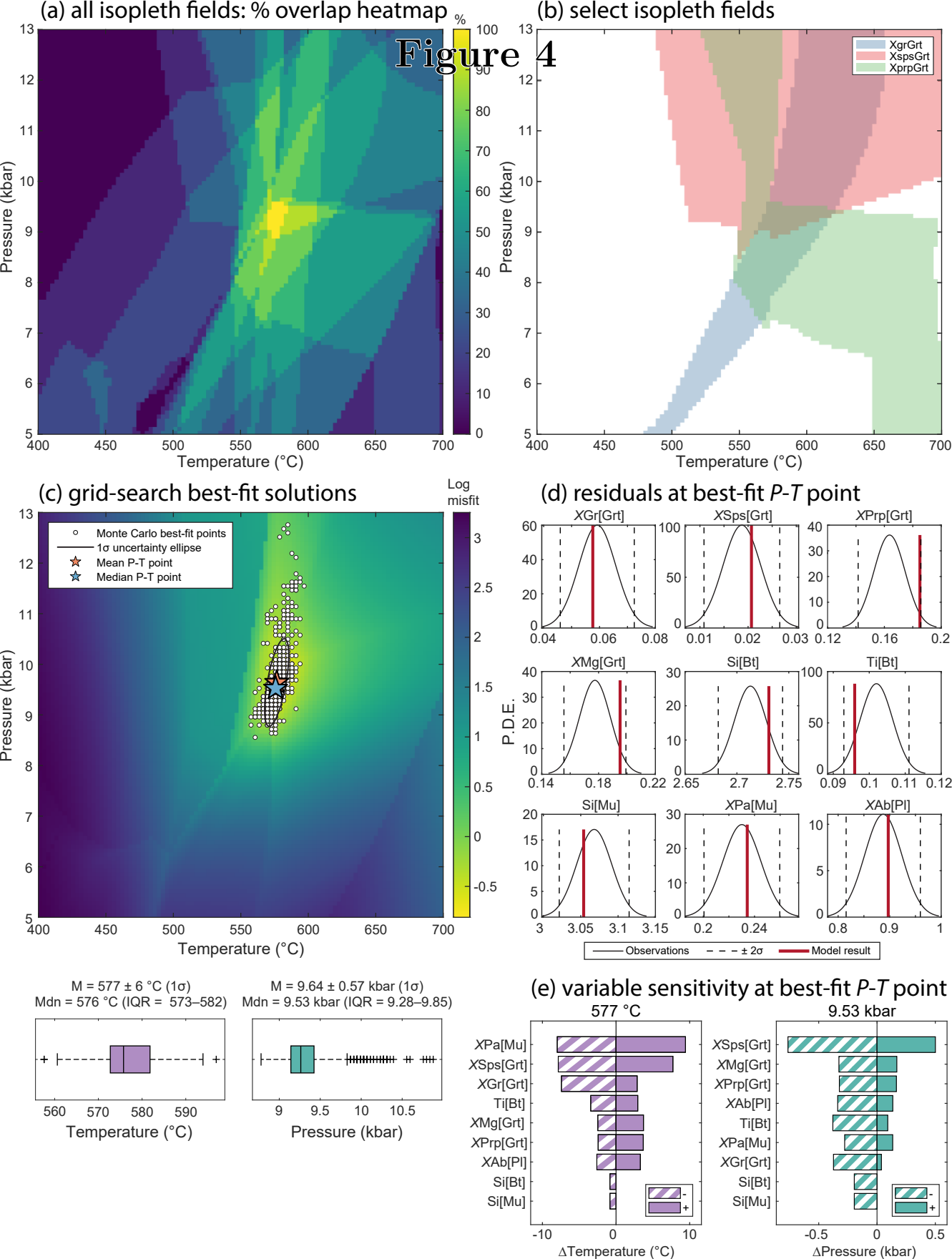
PI
 X_{Ab}

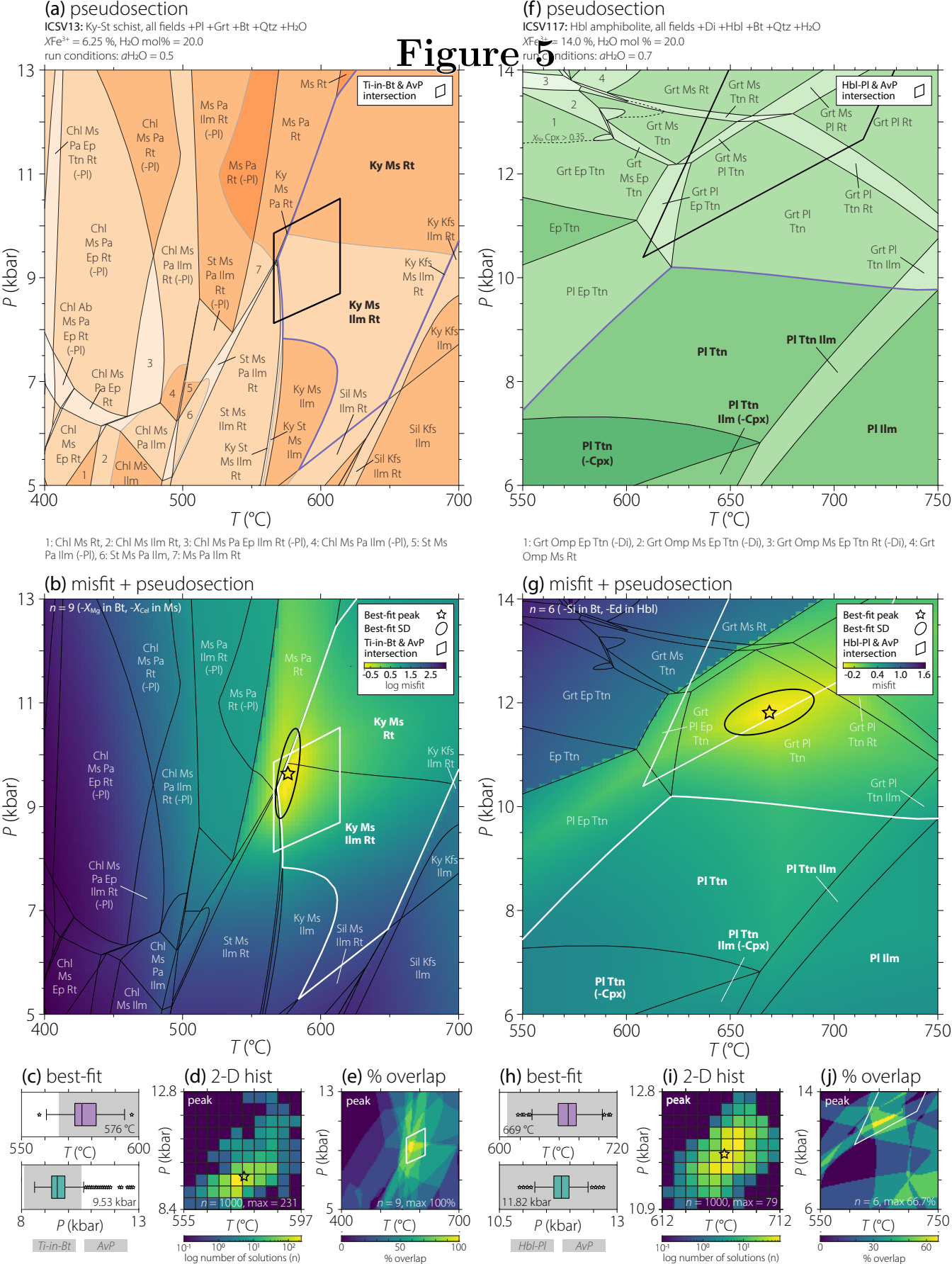
symbols

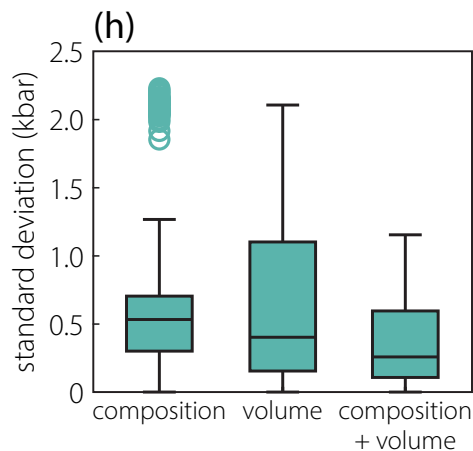
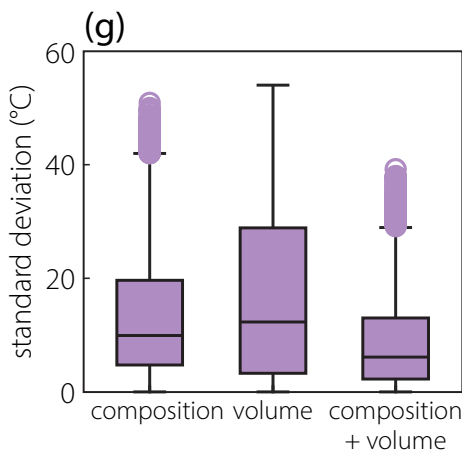
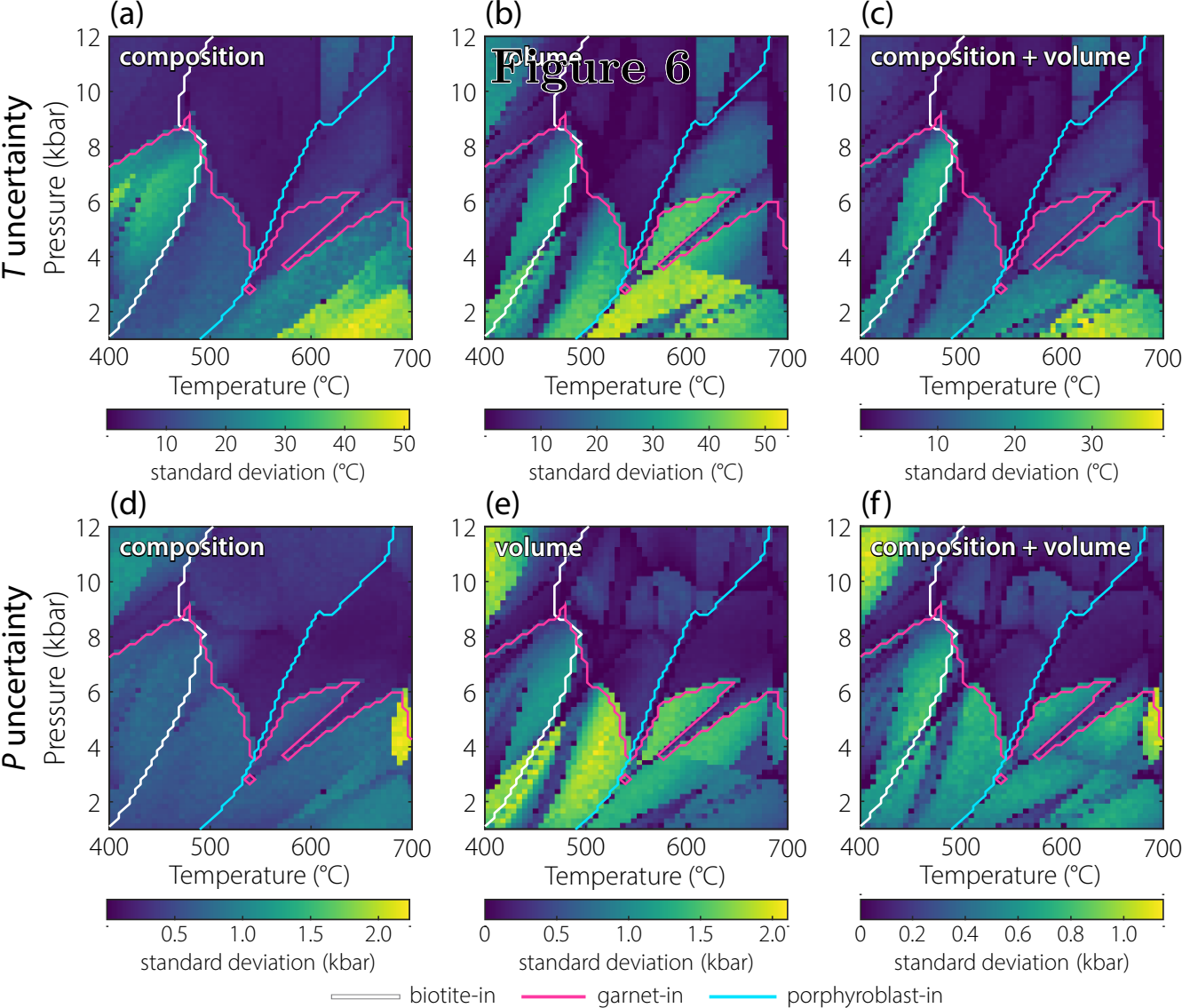
- ☆ peak result
- 1 sd ellipse
- ▭ assemblage field

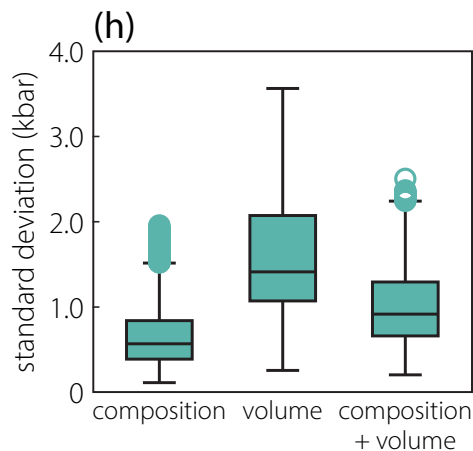
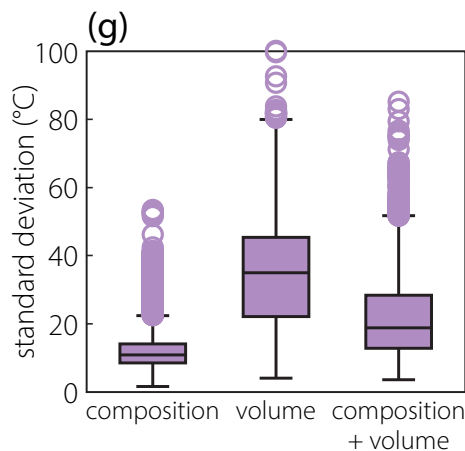
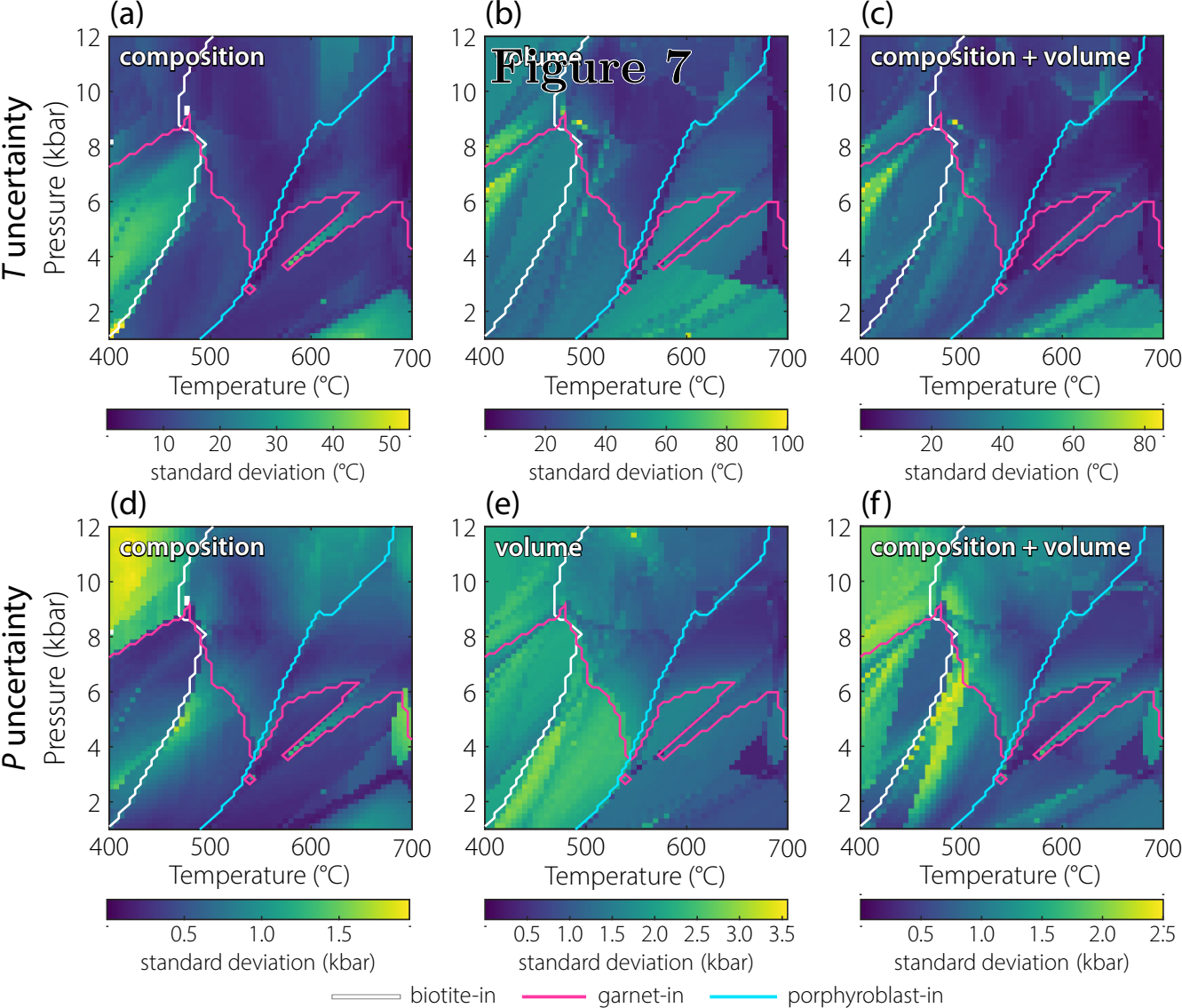
(a) best-fit P - T : grid-search inversion

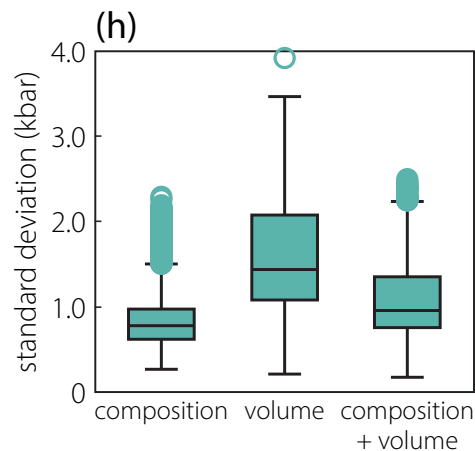
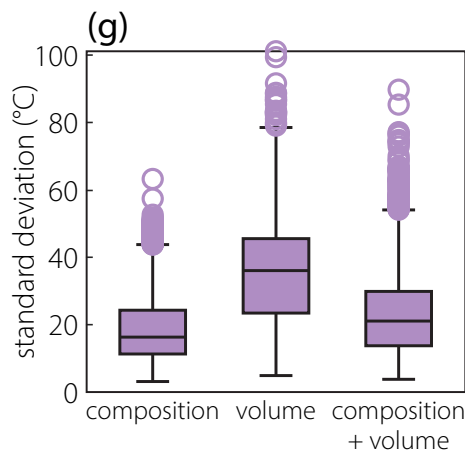
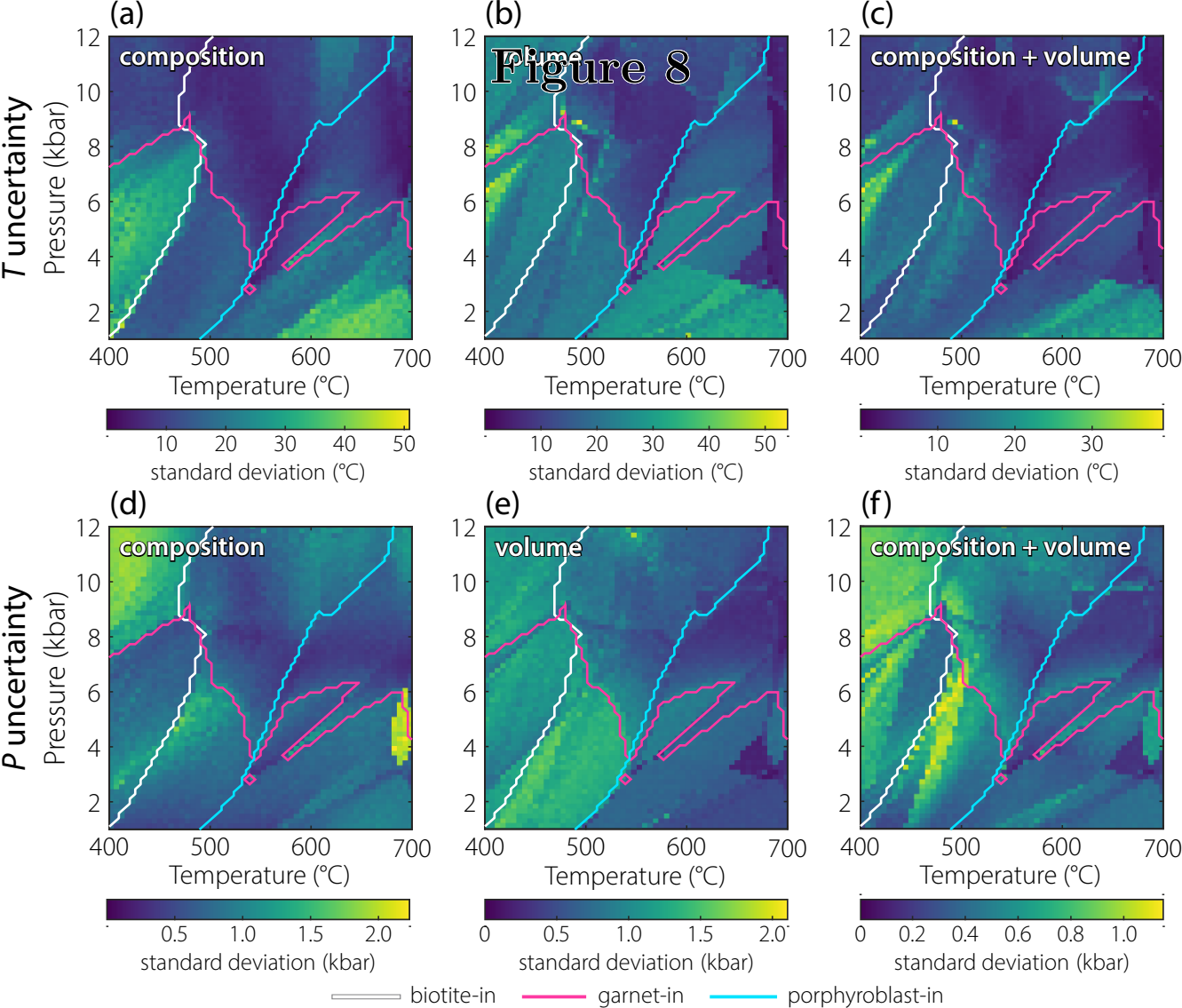


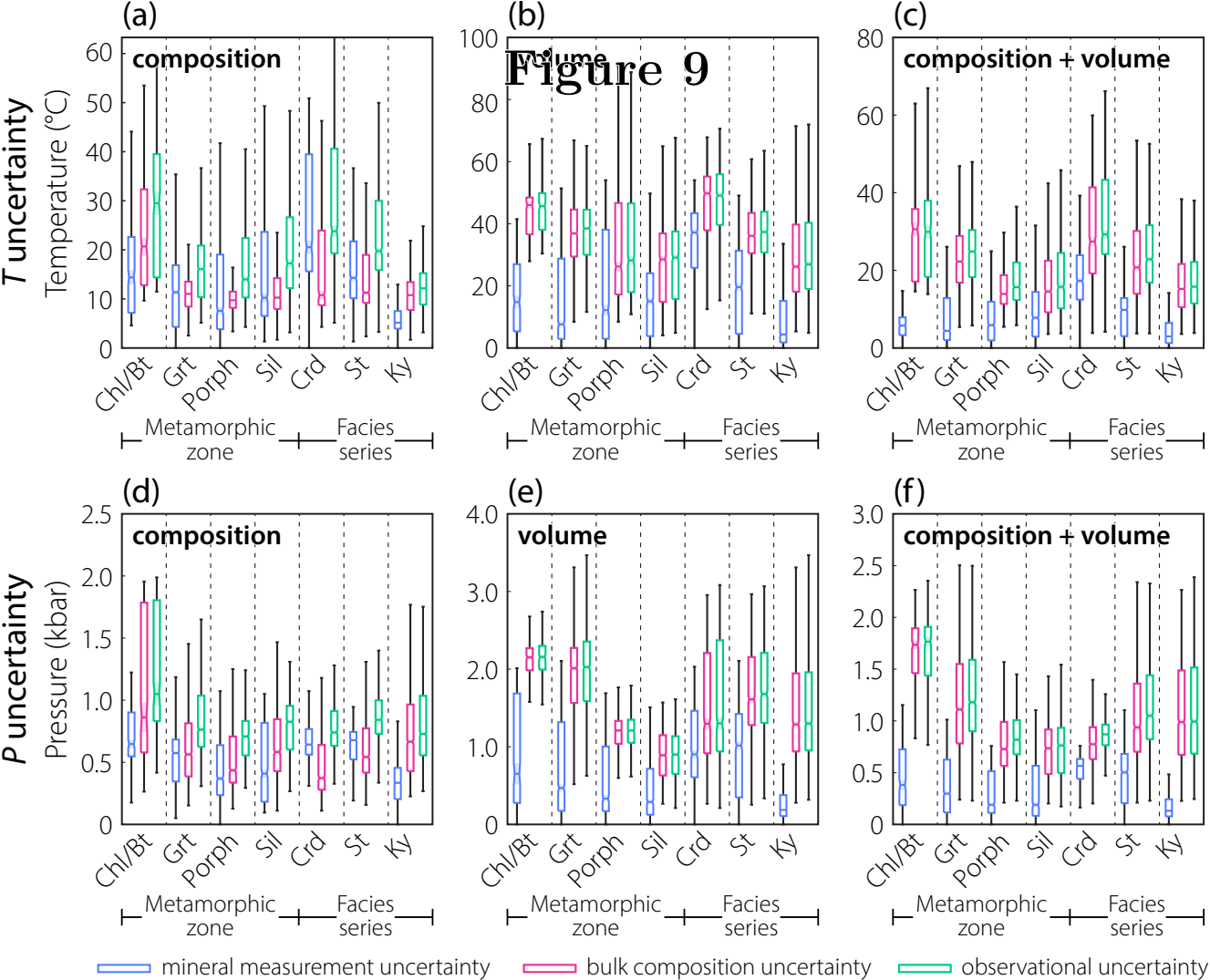


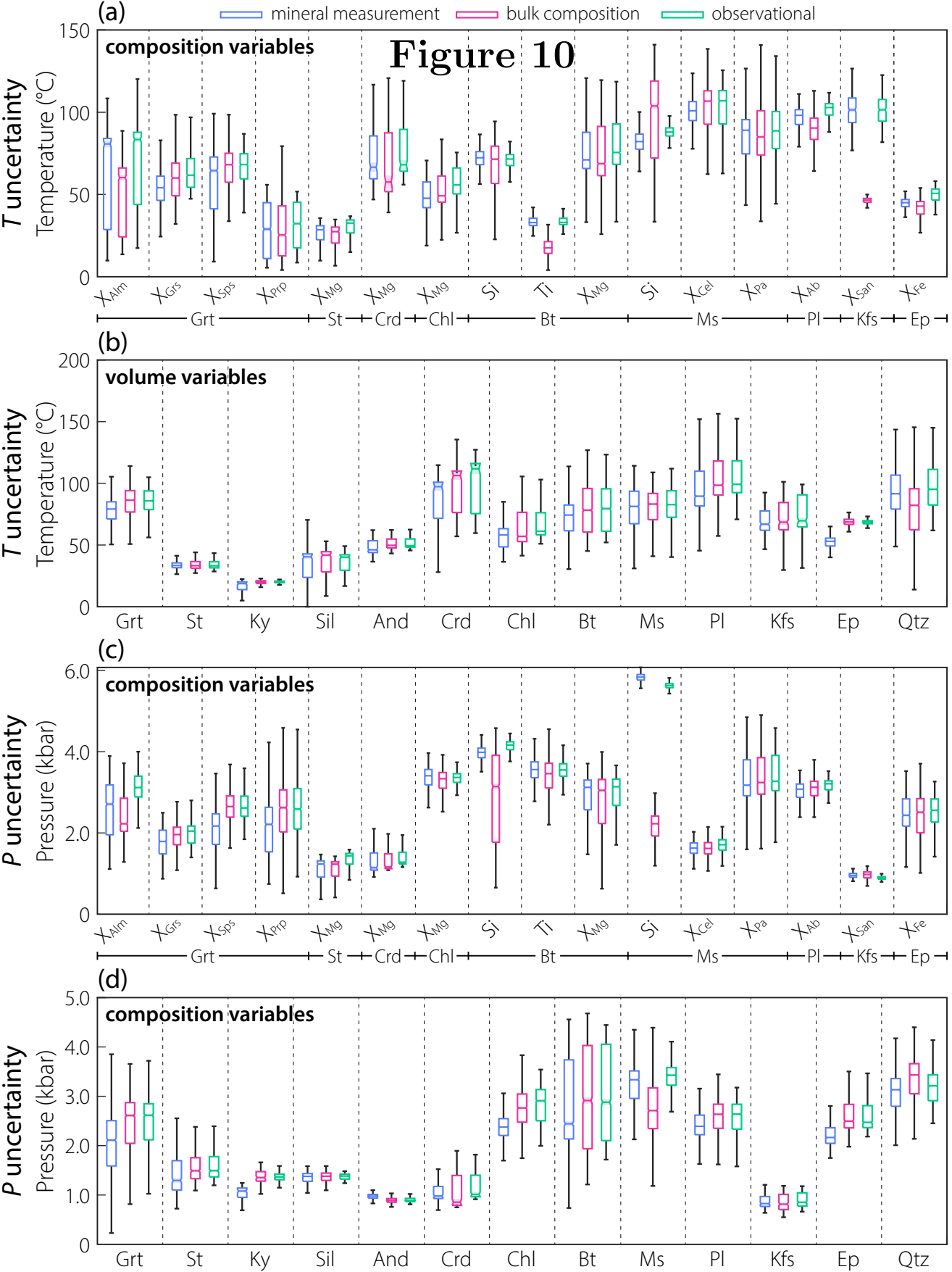












(b)

Figure 11

Volume

Bt Grt St Liq

Temperature (°C)

400 500 600 700

